# Nanoscale

Accepted Manuscript


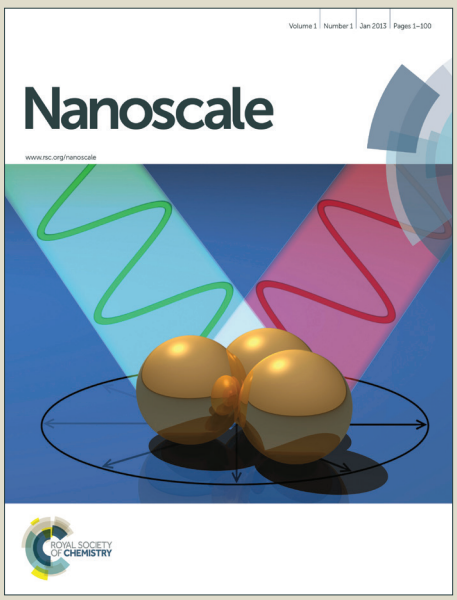





ROYAL SOCIETY OF CHEMISTRY

www.rsc.org/nanoscale

Cite this: DOI: 10.1039/c0xx00000x

www.rsc.org/xxxxxx

FEATURE ARTICLE

# Graphene-based nanocomposite anodes for lithium-ion batteries

**Weiwei Sun,[a] and Yong Wang*[a]**

***Received (in XXX, XXX) Xth XXXXXXXXX 20XX, Accepted Xth XXXXXXXXX 20XX***

**DOI: 10.1039/b000000x**

Graphene-based nanocomposites have been demonstrated as promising high-capacity anodes for lithium ion batteries to satisfy the ever-growing demands for higher capacities, longer cycle life and better high-rate performances. The synergetic effects between graphene and the introduced second-phase component are generally observed. In this feature review article, we will focus on the recent work of four different categories of graphene-based nanocomposites anodes by us and others: graphene-transitional metal oxide, graphene-Sn/Si/Ge, graphene-metal sulfide, graphene-carbon nanotube. For the supported materials on graphene, we will emphasize on the non-zero dimensional (non-particle) morphologies such as two dimensional nanosheet/nanoplate, one dimensional nanorod/nanofibre/nanotube. The synthesis strategies and lithium-ion storage properties of these highlighted electrode morphologies are distinct from the commonly obtained zero dimensional nanoparticles. We aim to stress the importance of the structure matching in the composites and their morphology-dependent lithium-storage properties and mechanisms.

.

## 1 Introduction

With the increasing demand for the ever-growing energy consumption, renewable energy sources and efficient energy conversion have attracted tremendous attentions. Electrical energy storage systems have been regarded as a suitable solution for the efficient electricity use in micro-grids or smart-grids. Among various devices, lithium-ion battery (LIB) has been widely used as an attractive power source for popular mobile devices with many outstanding features including high energy density, no memory effect, long cycle life and environmental friendliness.[1-5] However, the current LIB technology cannot satisfy the ever-growing demand for large-scale applications such as electric vehicles and scalable electricity storage. Advanced electrode materials with higher energy density and power density must be explored. Among the potential anode materials for LIBs, a variety of metals[6-15], metal oxides[13-37], and metal sulfides[38-44], have been proposed and attracted more and more attentions due to their higher theoretical capacities than commercial graphite anodes. Different categories of nanostructured electrode materials for LIB have been reviewed.[6,8,13,16-20] These high-capacity anodes often suffer from poor cycliability and high-rate performances. This is mainly due to the poor electrical conductivity and large volume change occurred during cycling, which leads to the electrode pulverization and the loss of the electrical contact.

*Department of Chemical Engineering, School of Environmental and Chemical Engineering, Shanghai University, Shangda Road 99, Shanghai, 200444, P. R. China. E-mail: yongwang@ shu.edu.cn*

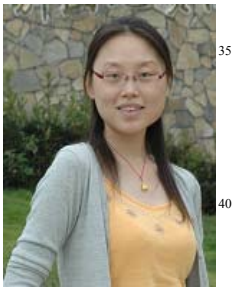

Weiwei Sun was born in 1982 and received her BS degree (2004) in chemistry from Shanxi Normal University and Ph.D. (2009) in chemistry from East China Normal University. She was a postdoctoral fellow in Fudan University, China and Wollongong University, Australia, before joining Shanghai University. She is currently a lecturer in Department of Chemical Engineering. Her research interests include materials for lithium ion batteries and hydrogen storage.

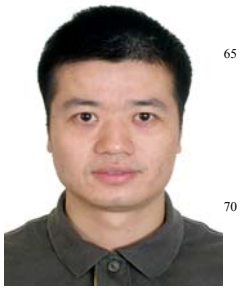

Yong Wang was born in 1976 and received his B Eng (1997) and M Eng (2000) in chemical engineering from Tianjin University, China, and Ph.D. (2004) in chemical engineering from National University of Singapore. He worked as a research fellow in Singapore-Massachusetts Institute of Technology Alliances from 2004 to 2006. He is currently a Professor and the Head of Department of Chemical Engineering, Shanghai University. His current research interests focus on nanomaterials for energy storage and environment.

In the past decade, various carbonaceous materials including graphite, meso/micro-porous carbon and carbon nanotube,[45-49] have been used as the matrix to support high-capacity electrodes, and such carbon-supported composites usually exhibit improved cycle life and high-rate performances compared to unsupported counterparts and enhanced capacity compared to carbons.[6,17-18]

Graphene, discovered in 2004,[50] is a single atomic planar two dimensional (2D) sheet, and owns unique physical and chemical properties.[51-53] The synthesis approaches and properties of graphene nanosheets (GNS) or reduced graphene oxide (RGO) have been reviewed with many details in previous articles,[54-56] and will not be described here. Compared with other carbonaceous materials, graphene shows unique merits such as a large theoretical specific surface area of 2620 $m^2 g^{-1}$, much higher than that of carbon nanotubes (CNTs) and graphite. Moreover, the high quality of the $sp^2$ carbon lattice of layer-by-layer graphene structure is very helpful for the electrons moving ballistically in the graphene layer even at ambient temperature.[54-56] Due to its unique single-atom layered structure, excellent electronic conductivity, strong mechanical strength, high flexibility, and good optical transparency, graphene nanosheets (GNS) have been applied in the field of energy harvesting and storage including lithium-ion batteries (LIBs), solar cells, supercapacitors, and fuel cells.[57-62] In particular, graphene was first reported as an anode for LIBs with a reversible capacity of 540 mAh $g^{-1}$,[57] followed by a number of reports using different synthesis strategies for graphene with Li-ion storage capacities of ~400-1100 mAh $g^{-1}$.[58-61] Because some of the reported capacities are substantially larger than the theoretical capacity of single-layer graphene (744 mAh $g^{-1}$ based on $Li_2C_6$), various mechanisms have been suggested for lithium ions storage such as both sides of graphene, micropores/defects, the expanded layer-spacing, layer edges, covalent sites, faradic capacitance, etc.[60-63] Meanwhile graphene can function as an ideal single-atom thick substrate for the growth of functional nanomaterials, [62-63] and it can also render them electrochemically more active. Unfortunately, easy restacking, large capacity loss in long cycles and poor dispersion in common solvents significantly restrict the use of graphene as the anode for LIB, thus ongoing research efforts focus on converting graphene sheets into functionalized graphene structures with different dimensions, and the introduction of the second-phase component (usually active high-capacity compounds) to prevent the restacking of few-layer GNS. When graphene-based composites are used as electrode materials for LIB, the following advantages are usually expected and demonstrated: 1) graphene nanosheets (GNS) can provide an elastic buffer space to accommodate the volume expansion/contraction of the supported materials during Li insertion/extraction process; 2) the 2D GNS structure can act as the support to immobilize the supported materials upon repetitive cycling and prevent their agglomeration; 3) GNS can increase the electrical conductivity of the supported materials and shorten the diffusion distance for electrons and lithium ions; 4) the porosity and defects generated in the composite can increase the electrode/electrolyte contact area and provide more active sites for lithium reaction and storage; 5) except for the beneficial effect of graphene to the supported high-capacity electrode materials, on the other hand, the latter can be regarded as a spacer to prevent the restacking of graphene to thick graphite platelet, therefore the promising properties relative to few-layer graphene structure can be preserved during repetitive cycling.

In this feature article, we summarize and provide critical discussions on the recent developments of graphene-supported nanocomposites for lithium ion storage including their synthesis strategies, morphology tuning and electrochemical performances. Depending on the distinct lithium storage mechanisms, four different types of graphene-supported nanomaterials: graphene-supported transitional metal oxides, graphene-supported Sn/Si/Ge-based oxides/alloys, graphene-supported metal sulfides and graphene-carbon nanotube based composites are presented. The supported materials often display different morphologies such as zero-dimensional (0D) nanoparticle, one-dimensional (1D) nanorod/nanofibre/nanotube, two dimensional (2D) nanosheet/nanoplate and three dimensional (3D) morphologies such as nanoflower. 0D nanoparticle is the most common product morphology for almost all kinds of electrodes due to its facile synthesis. In this review article, we would place more emphasis on the graphene-supported 1D, 2D and 3D nanostructures due to their advantages regarding the carefully-crafted morphology control, excellent structure affinity with graphene and generally good electrochemical properties.

## 2 Graphene-supported transitional metal oxides

Triggered by Tarascon's report[14], transitional metal oxides have been extensively studied as anode materials for LIBs [27-28,32-37]. A novel mechanism of "conversion reaction" has been identified, that is the reversible redox reaction between lithium and transitional metal oxides, as described below.

$$M_xO_y + 2ye^- + 2yLi^+ \leftrightarrow x[M]^0 + yLi_2O$$

When M is a transitional metal such as Ni, Co, Cu, Fe and Mn, the final product would be a homogeneous distribution of metal nanoparticles embedded in a $Li_2O$ matrix. Catalyzed by the transitional metal, reversible $Li_2O$ decomposition reaction provides outstanding lithium storage capability.[14] Transitional metal oxides can offer intriguing gravimetric capacities, which are two to three times as large as that of commercial graphite (372 mAh $g^{-1}$).[28] The lithium insertion and extraction occur at a more positive voltage (~0.5-2 V), which can reduce the safety concern of lithium plating, but the battery power is also reduced. The major drawback with this class of materials is an unsatisfactory cycling performance which is ascribed to the volume expansion during lithium insertion and their poor electronic conductivity.[32-37] Generally, nanostructured electrodes of transitional metal oxides can achieve significant improvement on the electrochemical properties compared with bulk transitional metal oxides. With the introduction of graphene as a perfect matrix to support transitional metal oxides, the graphene-supported composites show further improved cycling performances and high-rate performances.[28]

### 2.1 Nickel oxide

Nickel oxide (NiO), with a large theoretical capacity of 718 mAh $g^{-1}$, high safety, and low cost, has been proposed as a promising anode material for LIBs among transitional metal oxides.[27,28] In

the past decade, there are a number of reports concerning graphene-supported NiO composites with various structures, such as NiO nanoparticle[64-67], NiO nanosheet/nanoplate[68-74] and 3D NiO carnation[75].

NiO nanosheets were first prepared on graphene nanosheets (GNS) by a facile hydrothermal method and NiO nanoparticles were obtained by a similar process by using graphene oxide(GO) instead of GNS.[68] The schematic sketch of the growth process is illustrated in Fig. 1a. It is believed that NiO crystal growth is significantly affected by abundant oxygen-containing groups such as carboxyl and hydroxyl (confirmed by XPS) on GO, which hinders the nucleus growth into nanosheet structure. In such NiO-graphene sheet-on-sheet composites, a few NiO nanosheets with the size of 0.5-2 μm and thickness of 30-50 nm can be uniformly dispersed on GNS (Fig. 1b) by a possible binding interaction between residual carboxyl and/or hydroxyl groups of GNS and hydrated NiO. Fig. 1c shows a uniform dispersion of 2-5 nm NiO nanoparticles on GNS. A synergetic effect between GNS and NiO nanosheets can be demonstrated for Li-ion storage applications. The NiO-graphene sheet-on-sheet structure shows large reversible capacities (1056-1031 mAh $g^{-1}$ in 40 cycles at 71.8 mA $g^{-1}$) and excellent rate capabilities (large capacities of 872, 657, and 492 mAh $g^{-1}$ at large current rates of 718 mA $g^{-1}$ (1 C), 1436 mA $g^{-1}$ (2 C) and 3590 mA $g^{-1}$ (5 C), respectively). These electrochemical performances are much better than those of bare NiO nanosheets or NiO-graphene particle-on-sheet composite as shown in Fig. 1e. It is proposed that NiO nanosheet is a better "separator" material than nanoparticle regarding the separation and stabilization of GNS due to a larger contact area between these two types of similar 2D structures in sheet-on-sheet composite. Moreover, nanoparticles are more inclined to be aggregated compared to nanosheets with micrometer sizes. The sheet-like NiO structure has been demonstrated to remain intact after cycling as indicated in Fig. 1d.

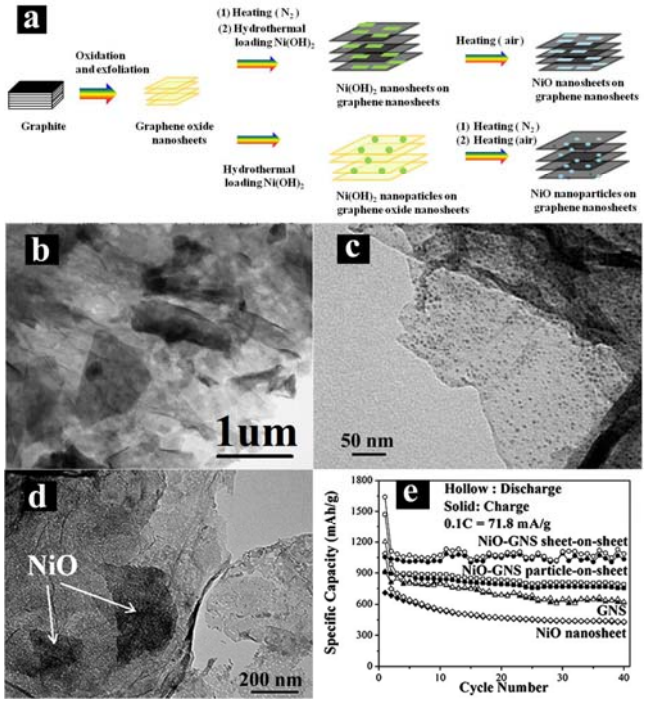


**Fig. 1** (a) Schematic illustration of the growth process of NiO-GNS sheet-on-sheet and nanoparticle-on-sheet composites. TEM images of (b) NiO-GNS sheet-on-sheet and (c) nanoparticle-on-sheet nanocomposites. (d) TEM image of the stable NiO nanosheet in sheet-on-sheet composites after 40 cycles. (e) Cycling performances of the composites at 71.8 mA $g^{-1}$ (0.1 C). Reproduced with permission from ref. 68. Copyright RSC 2011.

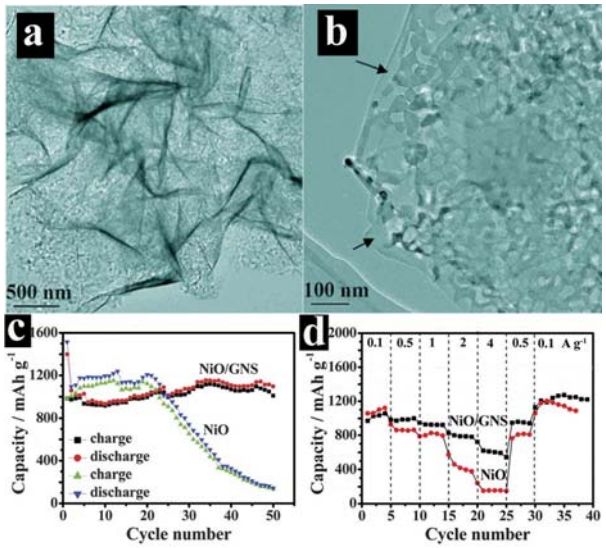


**Fig. 2** TEM images of (a) NiO nanosheet and (b) porous NiO-GNS sheet-on-sheet. (c) Cycling performances at 100 mA $g^{-1}$. (d) Rate capability performances at currents of 0.1-4 A $g^{-1}$. Reproduced with permission from ref. 72. Copyright RSC 2012.

GNS-supported porous NiO nanosheets/nanoplates also deliver outstanding electrochemical performances confirming the synergistic effect between porous 2D structure and conductive graphene.[72-74] As reported in Huang's article, [72] a unique ultrathin porous NiO nanosheets/graphene composite can be successfully self-assembled (Fig. 2a-b). A large reversible capacity of 1098 mAh $g^{-1}$ is retained after 50 cycles at a current density of 100 mA $g^{-1}$ with a good rate capability (615 mAh $g^{-1}$ at 4 A $g^{-1}$) (Fig. 2c-d). Xie and his co-workers also report a porous NiO nanosheets-wrapped GNS composite, which delivers a first-cycle charge capacity of 1467 mAh $g^{-1}$ and remains a reversible capacity up to 705 mAh $g^{-1}$ after 50 cycles at a current of 200 mA $g^{-1}$.[74]

The binding effect between NiO nanosheets and oxygenated graphene or graphene is very important for the stable sheet-on-sheet composite, which is explored by Zhou and co-workers.[70] The calculated adsorption energies are 1.37 and 1.84 eV for a Ni atom on oxygenated graphene with hydroxyl and epoxy, while 1.26 eV on graphene. More importantly, the corresponding calculated diffusion barriers (2.23 and 1.69 eV) of the Ni adatom on the oxygenated graphene surface are substantially larger than that on the graphene (0.19 eV). This indicates the C-O-Ni bridge works as an effective medium to make NiO nanosheets anchored strongly on graphene, which leads to a high reversible capacity and excellent cycling performances. Therefore by such a strong binding effect, the flexible and highly-conductive graphene can significantly improve the mechanical stability and electrical conductivity of the supported NiO materials.

A single 3D carnation-like NiO strucuture is grown on graphene by Tao and co-workers.[75] The obtained 3D hierarchical NiO-graphene composite exhibits a high reversible lithium storage capacity of 1065 mA h $g^{-1}$ after 50 cycles at a current density of 200 mA $g^{-1}$. The remarkable improvement of electrochemical performances has been attributed to the decrease of the volume expansion and contraction of NiO and the improvement of the electronic conductivity by the presence of graphene.

### 2.2 Cobalt oxide

For the GNS-supported cobalt oxides ($Co_3O_4$ and CoO), a variety of cobalt oxide morphologies including GNS-0D structure (nanoparticle)[76-83], GNS-1D structure (nanofibre[84] and nanorod/nanowire[85-87]), and GNS-2D (nanosheet/nanoplate) [88-92] can be obtained by different synthesis approaches. The physical contact area between these morphologies and GNS sheets can be regarded as point-to-point, line-to-line, and face-to-face respectively. The face-to-face contact should be more stable to immobilize the supported cobalt oxides on graphene by providing more contact area. Therefore, the GNS-2D structure (nanosheet/nanoplate) generally delivers more pronounced synergetic effect, for example, better Li-ion storage performances are observed due to the strong interfacial interactions between the supported 2D materials and GNS.

By a microwave-assisted synthesis method (Fig. 3a), porous $Co_3O_4$ nanosheets are fabricated on GNS to form a sheet-on-sheet nanostructure[88]. As shown in SEM (Fig. 3b) and TEM images (Fig. 3c), the micrometer-sized porous $Co_3O_4$ nanosheet structure is observed with pore sizes of 60-100 nm and the thickness around 100 nm. From the cycling performance comparison among GO, GNS, $Co_3O_4$-GNS sheet-on-sheet composites indicated in Fig. 3d, the $Co_3O_4$-GNS sheet-on-sheet composite shows the most prominent performance with the initial charge capacity of 1235 mAh $g^{-1}$ and a high charge capacity of 1065 mAh $g^{-1}$ after 30 cycles. Meanwhile, a capacity of 931 mAh $g^{-1}$ is observed at a large current rate of 5C (4450 mA $g^{-1}$) for the sheet-on-sheet structure. This capacity is still larger than the theoretical value of pristine $Co_3O_4$ (890 mAh $g^{-1}$). The observed higher-than-theoretical reversible capacity has been attributed to the lithium storage in nanocavities/defects in porous $Co_3O_4$-GNS composite and a possible faradic capacitance on the surface or edge planes.

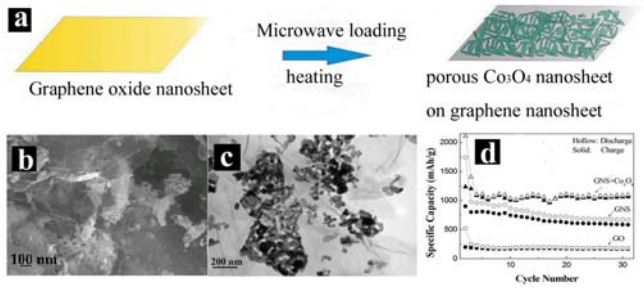


**Fig. 3** $Co_3O_4$-GNS sheet-on-sheet nanocomposite: (a) Schematic illustration of the growth process. (b) SEM image. (c) TEM image. (d) Cycling performances at 89 mA $g^{-1}$. Reproduced with permission from ref. 88. Copyright RSC 2010.

The sheet-on-sheet structure can be fabricated as a free-standing cobalt oxide/GNS film through a vacuum filtration and thermal treatment processes.[89] This film is self-assembled by cobalt oxide nanosheets and GNS under electrostatic interactions.[89] The cross-sectional SEM images, as shown in Fig. 4a and 4b, show that cobalt oxide nanosheets and GNS are tightly aligned in parallel to form an ordered layer structure in both $Co_3O_4$/GNS and CoO/GNS composites. However, the relative loosely stacked layered structure with abundant open voids and the porous $Co_3O_4$ nanosheets with a pore size of several nanometers existed in $Co_3O_4$/GNS film can deliver significantly increased surface area. Therefore the binder-free composite film achieves significant enhancement in Li-ion storage performances (~1400 mAh $g^{-1}$ at 100 mA $g^{-1}$) and cycling stability (~1200 mAh $g^{-1}$ at 200 mA $g^{-1}$ after 100 cycles), which is better than the traditional cobalt oxide/GNS composite in the presence of binder and carbon black (Fig. 4c and 4d). As another type of 2D structure, very thin $Co_3O_4$ nanoplates with diameters of ~20 nm and thicknesses of 1–2 nm are also prepared on graphene.[92] The nanoplate-on-sheet composite can deliver a large reversible capacity of 880 mAh $g^{-1}$ after 40 cycles at a current rate of 3 C.

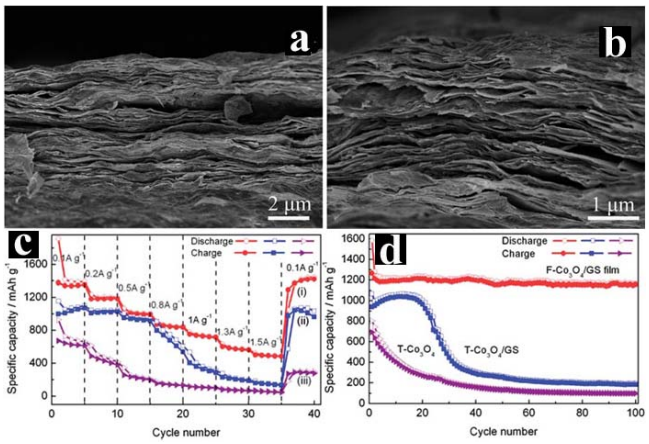


**Fig. 4** $Co_3O_4$ nanosheet/GNS film: (a-b) cross-sectional SEM images. (c) rate capabilities of binder-free composite, denoted as F-$Co_3O_4$/GS (i), traditional electrodes with binder: denoted as T-$Co_3O_4$/GS (ii) and T-$Co_3O_4$ (iii). (d) Comparative cycle performances of electrodes at 200 mA $g^{-1}$. Reproduced with permission from ref. 89. Copyright RSC 2013.

1D cobalt oxide morphologies are also prepared on GNS to form nanofibre-on-sheet[84] composite and nanowire/nanorod-on-sheet[85-87] composites. GO is mixed with the electrospun $Co_3O_4$ nanofibers to form a $Co_3O_4$-GNS composite paper by vacuum filtering, followed by hydrazine reduction.[84] In the absence of binder and carbon black, this film is directly used as an anode for LIB and shows a high reversible capacity of 840 mAh $g^{-1}$ after 40 cycles and a good rate capability. A number of $Co_3O_4$ nanorods (~500 nm in length and ~50 nm in diameter) are grown on graphene by hydrothermal method. The composite shows a reversible capacity of 907 mAh $g^{-1}$ at 0.1 C and a retained capacity of 844 mAh $g^{-1}$ after 50 cycles.[85] $Co_3O_4$ nanorods with large aspect ratio (30 nm in diameter and 1-2 micrometers in length) are obtained on GNS by a one-pot solvothermal method.[87] Very large reversible capacities of 1310 mAh $g^{-1}$ and 1090 mAh $g^{-1}$ are retained after 40 cycles at 100 mA $g^{-1}$ and 1000 mA $g^{-1}$, respectively.

### 2.3 Copper oxide

CuO material has been used as the active anode materials mainly due to its high theoretical lithium storage capacity (670 mAh $g^{-1}$), but its practical application is hindered by its fast capacity fading.[33-34,93-101] Recently, GNS-supported CuO nanocomposites with various nano/microstructures: nanoparticle-on-sheet[94-95], nanorod-on-sheet[96], spindle[97]/shuttle[98]-on-sheet, sheet-on-sheet[97,99], flower-on-sheet[100], and urchin-on-sheet[98,101] have been successfully synthesized. It is worthy noting that GNS-CuO with 2D nanosheet[97,99] and urchin/ shuttle-like structure[98,101], and hollow nanoparticle[93] show good lithium storage performances.

By similar solution-based synthesis approaches with different heating sources, reaction temperatures and solvents (Fig. 5a), three types of GNS-supported CuO composites with controlled morphologies: CuO-GNS sheet-on-sheet[97], CuO-GNS shuttle-on-sheet[98], and CuO-GNS urchin-on-sheet[98] have been obtained. TEM and HRTEM images of CuO-GNS shuttle-on-sheet composite as indicated in Fig. 5b, 5c and 5d illustrate that crystalline shuttle-like CuO nanostructures are uniformly distributed on GNS, forming a layer-by-layer structure, and this unique structure achieves highly-desired electrochemical performance with a very large capacity of 826 mAh $g^{-1}$ retained after 100 cycles at a large current of 700 mA $g^{-1}$. TEM image in Fig. 5e shows that CuO nanosheets are wrapped by GNS in the CuO-GNS sheet-on-sheet composite, while the urchin-like CuO nanostructures composed of numerous CuO nanoparticle nanoribbons with 20-30 nm in diameters in the urchin-on-sheet composite are shown in Fig. 5f. Under similar test conditions, the CuO/GNS sheet-on-sheet composite shows the best electrochemical performances[97] and the shuttle-on-sheet displays better performances than the urchin-on-sheet structure.[98] Therefore 2D CuO nanosheet is believed to be a perfect structure to be composited with 2D GNS.

GNS-supported CuO nanosheets can be also fabricated into a hybrid lamellar paper through vacuum filtration and hydrothermal reduction.[99] A large capacity of 737 mAh $g^{-1}$ can be retained after 50 cycles, which is much larger than that of bare GNS film paper (60 mAh $g^{-1}$) and pristine CuO nanosheets (219 mAh $g^{-1}$) afer same cycle number. Moreover, flower-like CuO/graphene composite[100] has been obtained by hydrothermal technique. These nanoflowers are composed of CuO nanosheets with an average diameter of 4.2 micrometers. The flower-on-sheet composite shows a reversible capacity of 603 mAh $g^{-1}$ at 0.1 C and 382 mAh $g^{-1}$ at 1 C, respectively.

Urchin-like CuO/graphene composite is also reported by a simple solution method in Wang's report.[101] Urchin-like CuO clusters with the average diameter of 1.5 μm are uniformly wrapped by a thin graphene layer (Fig. 6a-b). The composite exhibits enhanced electrochemical performance with very stable reversible capacities of ~600 mAh $g^{-1}$ at a current density of 65 mA $g^{-1}$ during 100 cycles (Fig. 6c-d).[101] The improvement of electrochemical properties have been mainly ascribed to the unique CuO urchin-like morphology and the electrically conductive graphene network, which can function as an elastic buffer.

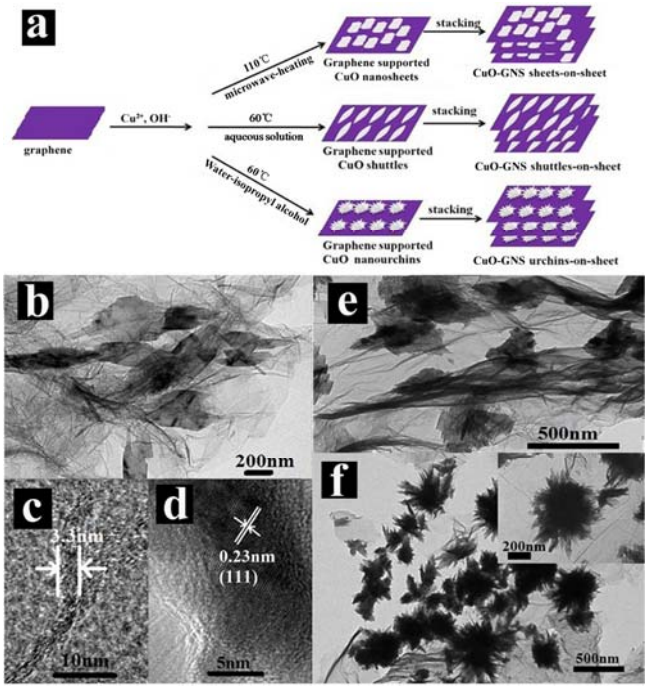


**Fig. 5** (a) Schematic illustration of the growth process of CuO-GNS sheet-on-sheet, shuttle-on-sheet and urchin-on-sheet structures. CuO-GNS shuttle-on-sheet composite: (b) TEM image, (c) HRTEM showing few-layer graphene, and (d) HRTEM image showing the lattice of CuO shuttle. (e) TEM image of CuO-GNS sheet-on-sheet. Reproduced with permission from ref. 97. Copyright RSC 2011. (f) TEM image of urchin-on-sheet composite. Reproduced with permission from ref. 98. Copyright Elsevier 2012.

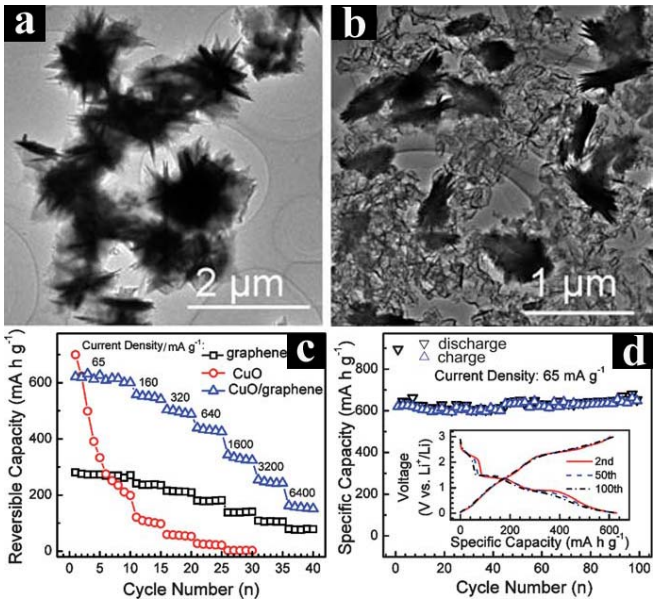


**Fig. 6** (a) TEM image of pristine CuO. (b) TEM image of CuO/graphene. (c) Rate-capabilities at various current densities. (d) Cycling performances of the CuO/graphene composite up to 100 cycles at a current of 65 mA $g^{-1}$. The inset figure shows the 2nd, 50th, and 100th discharge-charge curves. Reproduced with permission from ref. 101. Copyright RSC 2010.

### 2.4 Iron oxide

$Fe_2O_3$, a promising anode candidate for lithium ion batteries, owns high theoretical specific capacity of ~1005 mAh $g^{-1}$. However, it exhibits poor electronic conductivity and poor cycling performances upon long cycles.[35-37] The involvement of GNS in $Fe_2O_3$ systems has been proved to be an effective strategy, which offers increased mechanical stability, improved electrical contact and facilitated lithium diffusion.[102-118] Although a large number of efforts have been reported on GNS-supported iron oxides composites, most reports focus on GNS-supported $Fe_2O_3$ nanoparticle[102-109] or $Fe_3O_4$ nanoparticle[111-114]. Non-particle iron oxide morphologies such as nanosheet[115], nanorod[116] or nanorice[110]/spindle[117,118] have recently attracted more interest in the composite with GNS and showed improved structure-related Li-ion storage properties.

A fast microwave-assisted hydrothermal technique is used to fabricate $Fe_2O_3$-GNS rice-on-sheet nanocomposite[110], in which $Fe_2O_3$ nanorice is observed with length of 200 nm and diameters in a range from ~40 nm in the middle part to reduced 3-5 nm in the tip part (Fig. 7a). Large reversible charge capacities of 825, 762, and 633 mAh $g^{-1}$ are observed at large currents of 1, 2, and 5 C (1 C = 1000 mA $g^{-1}$), respectively. A high capacity of 582 mAh $g^{-1}$ at 1 C can be retained after 100 cycles. Compared to the particle-on-sheet composite, the $Fe_2O_3$-GNS rice-on-sheet composite exhibits a more stable cycle life (Fig. 7b). A similar $Fe_2O_3$-GNS nanospindle-on-sheet composite is prepared by a facile solvothermal method.[117] The obtained composite shows a large reversible capacity of 969 mAh $g^{-1}$ after 100 cycles at a current density of 100 mA $g^{-1}$.[117] A mixture of $Fe_2O_3$ 1D nanorods and nanoparticles are prepared on graphene by a hydrothermal route.[116] The composite can deliver an initial capacity of 771 mAh $g^{-1}$, which is retained at 565 mAh $g^{-1}$ after 30 cycles at a current rate of 0.1 C.[116] The poor reversible capacity should be ascribed to the presence of a large amount of $Fe_2O_3$ nanoparticles.

As shown in Fig 7c, we also fabricate a unique $Fe_2O_3$-GNS sheet-on-sheet nanostructure by a solvothermal technique.[115] The obtained $Fe_2O_3$ nanosheets are wrapped by GNS, forming a sandwich-like nanocomposite. As confirmed by BET measurements, the sheet-on-sheet composite exhibits a large surface area of 174 $m^2$ $g^{-1}$, which is over two times as large as that of the particle-on-sheet composite with same $Fe_2O_3$ loading. It is indicated that GNS is separated better by $Fe_2O_3$ nanosheet than $Fe_2O_3$ nanoparticle. The $Fe_2O_3$-GNS sheet-on-sheet composite exhibits a high reversible capacity of 1075 mAh $g^{-1}$ with good cycling performance at 0.1 C and a high reversible capacity of 622, 456, and 323 mAh $g^{-1}$ after 100 cycles at a high current rate of 1, 2, and 5 C, respectively. Notably, the corresponding particle-on-sheet composites can be easily obtained by adding structure directing agent[110] or varying reaction solvent[115]. These particle-on-sheet composites with same weight ratio of $Fe_2O_3$ to GNS are benchmarked with rice-on-sheet and sheet-on-sheet composites. The latter two composites show much better Li-ion storage properties than the corresponding particle-on-sheet composites under exactly same test conditions (Fig. 7b and 7d).

A flexible free-standing porous $Fe_3O_4$/GNS film paper is fabricated by a vacuum filtration technique,[118] in which hollow $Fe_3O_4$ nanospindles are embedded into the GNS network to

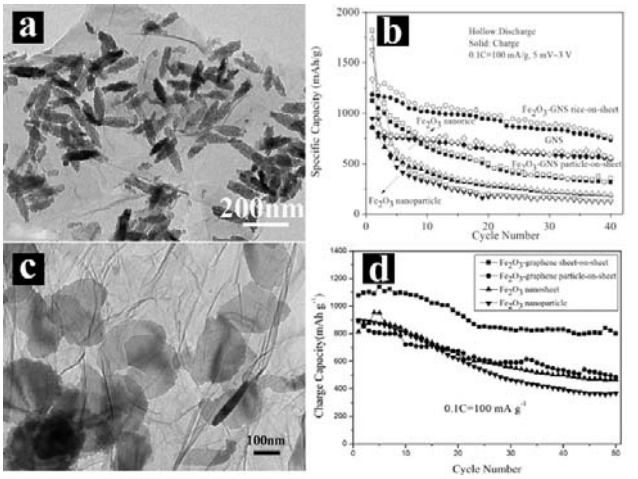


**Fig. 7** $Fe_2O_3$-GNS nanorice-on-sheet composite: (a) TEM image and (b) Cycling performances at 100 mA $g^{-1}$. Reproduced with permission from ref. 110, Copyright ACS 2011. $Fe_2O_3$-GNS sheet-on-sheet composite: (c) TEM image and (d) Cycling performances at 100 mA $g^{-1}$. Reproduced with permission from ref. 115. Copyright Nature 2013.

expand the interlayer space between the GNS layers, as shown in Fig. 8a-b. The special hollow structure allows the $Fe_3O_4$/GNS composite (39.6 wt% graphene) to deliver a high specific capacity of 1555 mAh $g^{-1}$ at 100 mA $g^{-1}$ and enhanced rate capability of 940 and 660 mAh $g^{-1}$ at 200 and 500 mA $g^{-1}$, respectively. The outstanding lithium-ion storage properties have been mainly attributed to the improved electrical contact of $Fe_3O_4$ by the three dimensional graphene network and the shortened pathway for both lithium ions and electrons in the porous electrode, in which volume change can be accommodated and electrolyte penetration can be facilitated. Notably, the electrochemical performances of the $Fe_3O_4$/graphene film paper without binder are much better than the traditional $Fe_3O_4$/GNS electrode with additional PVDF binder and carbon black as conductive agent (Fig. 8c-d). This improved electrochemical property has been mainly ascribed to the reduced resistance and enhanced electrode reaction kinetics in the film electrode.[118]

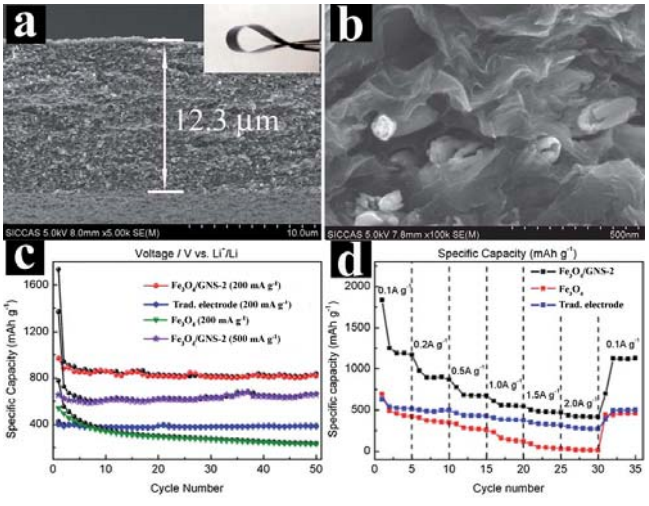


**Fig. 8** (a-b) Cross-section SEM images of the $Fe_3O_4$/GNS film and the inset figure in (a) is a digital photograph showing flexible $Fe_3O_4$-GNS film paper. (c) Cycling performances at 200 and 500 mA $g^{-1}$. (d) Rate capabilities. Reproduced with permission from ref. 118. Copyright. RSC 2013.

### 2.5 Other transitional metal oxides

There are still a number of reports on GNS-supported other transition metal oxides, such as manganese oxides[119-131], titanium oxides[132-146], vanadium oxides[147-163], molybdenum oxides[164-175], and zinc oxides[176-178], with applications as anode materials for LIB. For GNS-based manganese oxides composites anodes, 0D nanoparticle[119-125], 2D nanosheet[126]/nanoplate[127], and 1D nanoneedle[128]/nanorod[129]/nanotube[130]are all fabricated on GNS and explored for their Li-ion storage properties. Notably, crumpled graphene spheres with 3D open structure are prepared by capillary force induced by fast solvent loss in an aerosolization process and used to support $Mn_3O_4$.[123] Stable large reversible capacities of ~900 mAh $g^{-1}$ are achieved for $Mn_3O_4$-GNS sheet-on-sheet[126] and particle-on-sheet[119]. The most outstanding performance comes from the graphene supported ultrafine MnO nanoparticles.[131] An extremely large reversible capacity as high as 2014 mAh $g^{-1}$ can be observed after 150 cycles at 200 mA $g^{-1}$. This reversible capacity should be the largest one among all transitional metal oxides and their derivatives reported so far. Interfacial lithium ion storage, reconstructed nanostructure and interconnected graphene composite framework have been suggested as main causes for the distinguished synergetic effect. The shortened transportation length for Li-ions and electrons and facilitated kinetics of conversion reaction also result in excellent high-rate performances.

Different from other transitional metal oxides, $TiO_2$ displays a lithium insertion/extraction mechanism with the advantage of negligible structure variation during lithium intercalation and deintercalation.[18] In spite of its low theoretical capacity (337 mAh $g^{-1}$), $TiO_2$ has been proposed as a promising anode for electrical vehicles due to its stable structure, good safety and fast discharge and charge kinetics in modified $TiO_2$ with improved electronic conductivity and more exposed energetic facets. The presence of graphene can improve the poor electronic conductivity of $TiO_2$ anodes, thus enabling better high-rate performances. $TiO_2$-GNS composites with various structures have been reported, including 0D $TiO_2$ nanoparticle[132-138], 2D $TiO_2$ nanosheet[139-142], 1D nanobelt[143]/nanorod[144]/nanotube[145], and 3D $TiO_2$ nanoflower[146]. It should be noted that a unique $TiO_2$-GNS nanobelt-sheet hybrid nanostructure[143] shows outstanding electrochemical performances with an ultrahigh reversible capacity (over 430 mAh $g^{-1}$ at 0.15 A $g^{-1}$) and a superior high-rate capability (210 mAh $g^{-1}$ at 3 A $g^{-1}$) among various $TiO_2$-based anodes.

## 3 Graphene- Sn/Si/Ge-based nanocomposites

Sn/Si/Ge-based anode materials such as Sn-based alloys, Sn/Si/Ge-based oxides and Sn/Si/Ge-based composites have been extensively studied in the literature.[7,8,10-13,28-30] Tin (Sn) shows a high theoretical specific capacity of ~990 mAh $g^{-1}$, while that of silicon (Si) is 4200 mAh $g^{-1}$ because each Sn/Si can alloy and de-alloy with a maximum 4.4 Li. In comparison, every 6 carbon atoms can only intercalate 1 lithium. Because Sn is easily oxidized in air and $SnO_2$ is usually obtained and explored for Li-ion storage properties.[10-13,28-30] During the first cycle of lithium insertion, tin oxide is reduced to Sn metal and $Li_2O$. It is worthy pointing out that the obtained $Li_2O$ is usually believed to be impossible to decompose reversibly, which is different from transitional metal oxides. A large irreversible capacity loss is associated with this irreversible reaction. Upon the following cycles, tin oxide follows similar Li alloying and de-alloying storage mechanism indicated in the reversible reaction as described below:

$$M_xO_y + 2ye^- + 2yLi^+ \rightarrow x[M]^0 + yLi_2O$$

$$M + ze^- + zLi^+ \leftrightarrow Li_zM$$

The crucial problem with Sn/Si/Ge-based anodes is the huge volume change during lithium insertion and extraction process, for example, ~300% volume expansion for Sn. This would lead to the electrode pulverization and subsequently fast capacity fading for this class of anode materials. The use of graphene to support Sn/Si/Ge has been demonstrated as an effective strategy to solve the problem. The large volume change can be accommodated by flexible and conductive graphene. The suitable dispersion of Sn/Si/Ge-based anode among graphene nanosheets can also be helpful for keeping graphene nanosheet separated. Among various GNS supported Sn-based materials, as summarized with their lithium storage properties in Table 1, metallic tin tends to form 0D nanoparticle [179-185] or 1D nanorod/nanowire[186-188] or nanopillar[189] structure and a single example of 2D nanosheet morphology[190], but tin oxide can exhibit a variety of morphologies such as nanoparticle[191-219], nanosheet[220-221], nanorod/nanowire[222-224], and nanoflower[225]. The $SnO_2$@C core-shell structure[202,217,218] is also adopted to improve the electrical contact and accommodate the volume expansion of Sn core by a layer of disordered carbon shell. A large reversible capacity of 757 mAh $g^{-1}$ is achieved for the core-shell electrode structure after 150 cycles at 200 mA $g^{-1}$.[218] Furthermore, there are a few Sn–based alloys reported on graphene[226-231] and only Sn-based alloy-GNS nanoparticle-on-sheet morphology can be obtained due to the difficult control of bimetallic crystal structure (Table 1). In general, among numerous GNS supported Sn-based nanocomposite anode materials, $Sn/SnO_2$ tends to form the nanoparticle-like morphologies, which are proposed to be supported/wrapped/encapsulated on/by/in GNS due to its flexible and curled characteristics.[179-185,191-219] However, GNS-supported $Sn/SnO_2$ materials with some special morphologies such as 1D nanorod/nanowire[186-189,222-224] and 2D nanosheet[190,220-221] would show enhanced lithium storage properties due to strong interaction between the $SnO_2$ nanostructure and GNS nanosheets. For example, a large reversible capacity of 1107 mAh $g^{-1}$ is retained after 100 cycles for graphene-supported $SnO_2$ nanorods at a current density of 200 mA $g^{-1}$.[223] It should be noted that some GNS-supported $SnO_2$ composites with the involvement of modified graphene (such as, N-doped GNS[199,200,224,226], activated porous GNS[214], graphene aerogel[201], and graphene nanoribbons[196]) also exhibit wonderful electrochemical performances as the anode for lithium-ion batteries. A large capacity of 1346 mAh $g^{-1}$ can be achieved for N-doped graphene supported $SnO_2$ nanocrystals after 500 cycles at 0.5 A $g^{-1}$ and the composite also exhibits a large reversible capacity of ~417 mAh $g^{-1}$ at an extremely large current of 20 A $g^{-1}$.[200] Lastly, some examples of GNS-supported $Sn/SnO_2$ nanoparticles with good control of interaction between two components in the composites can also achieve excellent lithium storage properties, which are also listed in Table 1.

**Table 1** GNS-supported Sn-based nanostructures and their electrochemical properties for LIBs.

| Sn/$SnO_2$/alloy morphology | Composite | Electrochemical Performances | Ref. |
|---|---|---|---|
| Nanosheets | Sn+GNS | A large initial discharge capacity of 1380 mAh $g^{-1}$ with initial Coulombic efficiencies of 66.5% and the retained capacity of 590 mAh $g^{-1}$ after 60 cycles at 50 mA $g^{-1}$ | 190 |
| | $SnO_2$+GNS | A high reversible capacity of 518 mAh $g^{-1}$ at 400 mA $g^{-1}$ after 50 cycles with only 0.51% capacity loss per cycle | 220 |
| | $SnO_2$+GNS | The first reversible charge capacity of 975 mAh $g^{-1}$ and the retained capacity of 451 mAh $g^{-1}$ at 100 mA $g^{-1}$ after 100 cycles | 221 |
| Nanopillars | Sn+GNS | An initial reversible capacity of 734 mAh $g^{-1}$ and the reversible capacities are preserved at about 723 and 679 mAh $g^{-1}$ (98.4 and 92.5% retention rates from the first cycle) after 15 and 30 cycles, respectively. | 189 |
| Nanorods /nanowires | Sn@GNS | A reversible specific capacity of 846 mAh $g^{-1}$ after 100 cycles at the current density of 200 mA $g^{-1}$ and a reversible capacity of 488 mAh $g^{-1}$ at 2 A $g^{-1}$ | 188 |
| | $SnO_2$+GNS | The second discharge capacities of 907 and 659 mAh $g^{-1}$ at 100 and 200 mA $g^{-1}$ and the retained reversible capacities of 710 and 574 mAh $g^{-1}$ at 100 and 200 mA $g^{-1}$ after 50 cycles, respectively | 222 |
| | $SnO_2$+GNS | The reversible capacity of 1107 mAh $g^{-1}$ after 100 cycles at a current density of 200 mA $g^{-1}$,corresponding to 96.2% of the initial value | 223 |
| | $SnO_2$+N-doped GNS | The reversible capacities of 901, 774, and 506 mAh $g^{-1}$ after 50 cycles at current densities of 100 , 200 and 1000 mA $g^{-1}$ respectively with the capacity loss of ~0.4% per cycle at 100 and 200 mA $g^{-1}$ and ~0.2% per cycle at 1000 mA $g^{-1}$ | 224 |
| | Sn@CNT+GNS | A very large initial charge capacity of 1160 mAh $g^{-1}$ at 100 mA $g^{-1}$ and a large reversible capacity of 982 mAh $g^{-1}$ retained after 100 cycles | 186 |
| | Sn@CNT+GNS | The reversible specific capacities of ~760 mAh $g^{-1}$ in the initial 10 cycles and 630 mAh $g^{-1}$ after 50 cycles at 100 mA $g^{-1}$ | 187 |
| nanoflowers | $SnO_2$@GNS | The first discharge and charge capacity are 1588 and 1240 mAh $g^{-1}$ at 50 mA $g^{-1}$, respectively and the retained capacity of 730 mAh $g^{-1}$ after 40 cycles | 225 |
| nanoparticles | $SnO_2$@S+GNS | A reversible capacity of 819 mAh $g^{-1}$ after 200 cycles at 500 mA $g^{-1}$ and an excellent rate capability of 580 mAh $g^{-1}$ at a high current density of 4000 mA $g^{-1}$ | 198 |
| | $SnO_2$@C+GNS | A capacity of 757 mAh $g^{-1}$ after 150 cycles at 200 mA $g^{-1}$ | 218 |
| | $SnO_2$@C+GNS | A capacity of 703 mAh $g^{-1}$ after 80 cycles at 100 mA $g^{-1}$ and the retained capacity of 443 mAh $g^{-1}$ after 100 cycles at 1000 mA $g^{-1}$ | 217 |
| | $SnO_2$@C+GNS | An initial reversible charge capacity of ~862 mAh $g^{-1}$ at 200 mA $g^{-1}$ and the retained capacity of 622 mAh $g^{-1}$ after 100 cycles | 202 |
| | $SnO_2$+CNT+GNS | A capacity of 502 mAh $g^{-1}$ after 50 cycles at 100 mA $g^{-1}$ and a capacity of 344 mAh $g^{-1}$ retained even at 1000 mA $g^{-1}$ | 203 |
| | $SnO_2$+CNT+GNS paper | Initial reversible capacities of 345 and 635 mAh $g^{-1}$ at 1.5 and 0.25 A $g^{-1}$ respectively and a reversible capacity of 387 mAh $g^{-1}$ after 50 cycles at 0.1 A $g^{-1}$ | 216 |
| | $SnO_2$+PANI+GNS | A reversible capacity larger than 573 mAh $g^{-1}$ over 50 cycles with Coulombic efficiency of 99.26%, which amounts to 73.7% of its theoretical specific capacity | 215 |
| | $Co_3Sn_2$@Co+ N-doped GNS | A high capacity of 1615 mAh $g^{-1}$ at 250 mA $g^{-1}$ after 100 cycles with excellent capacity retention of 102% and the reversible capacity of 794 mAh $g^{-1}$ at 2.5 A $g^{-1}$ and Coulombic efficiencies approaching 100% | 226 |
| | $CoSn_2$+GNS | The reversible capacity is close to 450 mAh $g^{-1}$ after 35 cycles at 50 mA $g^{-1}$. | 227 |
| | $Cu_6Sn_5$+GNS | A reversible capacity of 411 mAh $g^{-1}$ after 1600 cycles at 500 mA $g^{-1}$ and the reversible capacity is as large as 220 mAh $g^{-1}$ at 10 A $g^{-1}$ | 228 |
| | SnCo+GNS | An initial large reversible capacity of 1117 mAh $g^{-1}$ at a current density of 72 mA $g^{-1}$ and the retained 571 mAh $g^{-1}$ after 60 cycles | 229 |
| | SnSb@C+GNS | A large reversible capacity of 896 mAh $g^{-1}$ after 30 cycles corresponding to 91.6% of the first-cycle value and a good rate capability (an initial reversible capacity of 668 mAh $g^{-1}$ observed at a large current of 4 A $g^{-1}$) | 230 |
| | SnIn+GNS | A reversible capacity of 865 mAh $g^{-1}$ at 100 mA $g^{-1}$ with 83.9% capacity retention after 50 cycles and good rate capability (493 mAh $g^{-1}$ at 600 mA $g^{-1}$ after 25 cycles) | 231 |
| | $SnO_2$+Graphene Aerogel | A reversible capacity of ~590 mAh $g^{-1}$ at 100 mA $g^{-1}$ after 80 cycles corresponding to 64% of the initial reversible capacity | 201 |
| | $SnO_2$+Activated GNS | A capacity of up to 610 mAh $g^{-1}$ at 100 mA $g^{-1}$ after 50 cycles and good rate-performance of 889, 747, 607, 482 and 372 mAh $g^{-1}$ at 100, 200, 500, 1000, and 2000 mA $g^{-1}$, respectively | 214 |
| | $SnO_2$+N-doped GNS | A large capacity of 1220 mAh $g^{-1}$ after 100 cycles at 90 mA $g^{-1}$ corresponding to 65% of first-cycle charge capacity of 1890 mAh $g^{-1}$ | 199 |
| | $SnO_2$+N-doped GNS | A large capacity of 1346 mAh $g^{-1}$ after 500 cycles at 0.5 A $g^{-1}$ and excellent high-rate performances (~417 mAh $g^{-1}$ at an extremely large current of 20 A $g^{-1}$ | 200 |
| | $SnO_2$+GNS | A stable capacity of 890 mAh $g^{-1}$ after 80 cycles at 500 mA $g^{-1}$ and good high-rate performance (790 mAh $g^{-1}$ remained when cycled at a high current density of 1 A $g^{-1}$) | 191 |
| | $SnO_2$+GNS | A large capacity of 821 mAh $g^{-1}$ after 194 cycles with excellent cycling stability | 192 |
| | $SnO_2$+GNS | A high reversible capacity of 872 mAh $g^{-1}$ after 200 cycles at 100 mA $g^{-1}$ | 193 |
| | $SnO_2$+GNS | An initial reversible charge capacity of 1924 mAh $g^{-1}$ and the retained capacity of 1546 mAh $g^{-1}$ at 1 A $g^{-1}$ after 40 cycles | 194 |
| | $SnO_2$+GNS | An initial charge capacity of 1255 mAh $g^{-1}$ at 100 mA $g^{-1}$and the retained capacity of 986 mAh $g^{-1}$ after 30 cycles | 195 |
| | $SnO_2$+Graphene Nanoribbon | An initial charge capacity of 1130 mAh $g^{-1}$ and the retained capacity of ~825 mAh $g^{-1}$ after 50 cycles at 100 mA $g^{-1}$ | 196 |
| | $SnO_2$+GNS | An initial charge capacity of ~1000 mAh $g^{-1}$ and good capacity retention of 594 mAh $g^{-1}$ up to the 50th cycle at a current density of 100 mA $g^{-1}$ | 197 |
| | $SnO_2$+GNS | An initial charge capacity of 690 mAh $g^{-1}$ at 100 mA $g^{-1}$ and the retained capacity of 433 mAh $g^{-1}$ after 20 | 219 |

| | | |
|---|---|---|
| | cycles | |
| Sn+GNS | A reversible capacity of 466 mAh $g^{-1}$ at a current density of 879 mA $g^{-1}$ (1 C) after over 4000 cycles and 794 mAh $g^{-1}$ at 293 mA $g^{-1}$ (1/3 C) after 400 cycles | 179 |
| Sn+GNS | An initial large charge capacity of 946 mAh $g^{-1}$ at a large current density of 1600 mA $g^{-1}$ and the retained capacity of 542 mAh $g^{-1}$ after 30 cycles | 180 |
| Sn+GNS | An initial large charge capacity of 1037 mAh $g^{-1}$ at 150 mA $g^{-1}$ and the retained capacity of 1005 mAh $g^{-1}$ after 120 cycles. A stable capacity of ~400 mAh $g^{-1}$ after 5000 cycles at a large current of 3.6 A $g^{-1}$ | 183 |
| Sn+GNS | An initial large charge capacity of ~810 mAh $g^{-1}$ at 55 mA $g^{-1}$ and the retained capacity of 508 mAh $g^{-1}$ after 100 cycles | 184 |

Development of Sn-based materials with carefully crafted nanostructure is very useful to ensure good cycling performances. A unique hierarchical Sn@CNT nanostructure rooted in GNS is synthesized from the intermediate of $SnS_2$ nanoparticles on GO sheets.[186] The advantages of Sn@CNT-GNS composite can be illustrated in the growth process as indicated in Fig. 9a. The CNT overlayer around the filled Sn can offer a better electrical contact and is used to buffer and confine the volume change of Sn materials with the assistance of the GNS substrate, thus improving the structure stability of Sn during cycling. It is worthy noting that the uniform CNT shells (thickness of 6-10 nm), which are filled with Sn nanorods as the filler cores and tightly integrated with GNS by the junction in such a composite. The unique morphology of the Sn@CNT-GNS nanostructure leads to an extremely larger initial reversible charge capacity of 1160 mAh $g^{-1}$ than those of GNS, $SnS_2$ particle, and GNS supported $SnS_2$ nanopaticle. A large reversible capacity of 982 mAh $g^{-1}$ can be retained after 100 cycles for the composite (Fig. 9b). The high-rate cycling performance as shown in Fig. 9c reveals the GNS-Sn@CNT is cycled very well with high initial reversible capacities of 828, 686, and 594 mAh $g^{-1}$ at 1C, 2C, and 5C (1C = 1000 mA $g^{-1}$), respectively.

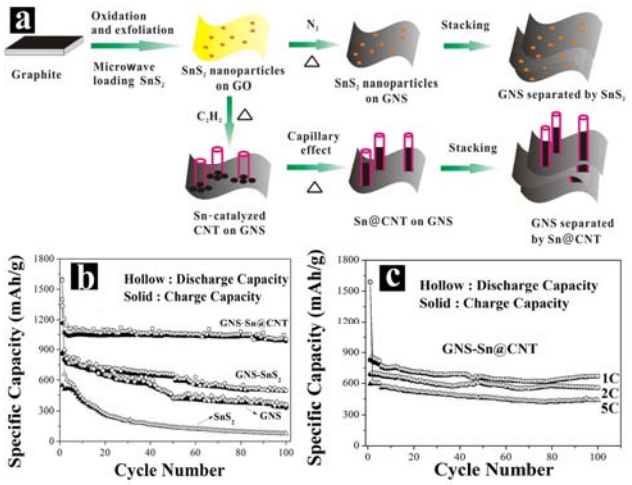


**Fig. 9** CNT-encapsulated Sn nanorods rooted in GNS (Sn@CNT-GNS): (a) Schematic illustration of the growth process. (b) Cycling performance at 0.1 C. (c) High-rate cycling performances at 1-5 C, 1C=1000 mA $g^{-1}$. Reproduced with permission from ref.186. Copyright ACS 2011.

According to a facile thermal reduction process, a 3D porous graphene-confined Sn nanosheet composite[190] is reported, which consists of GNS/Sn nanosheet/GNS nano-units as shown in SEM and TEM images of Fig. 10 a-b. Two ultrathin Sn nanosheets can be observed on GNS in TEM image of Fig. 10c. The cross-section of the sandwiched GNS/Sn nanosheets/GNS can be clearly indicated in TEM image of Fig. 10d, in which Sn nanosheets (~10 nm in thickness) is sandwiched between two graphene nanosheets (~5 nm in thickness). The closely-contacted GNS and Sn nanosheets may greatly facilitate the lithium alloying and de-alloying reactions with Sn and prevent GNS aggregation. This novel GNS supported Sn nanosheets exhibit large reversible capacity and good cycling performances of above 800 mAh $g^{-1}$ in the initial 10 cycles and ~590 mAh $g^{-1}$ after 60 cycles at a current density of 50 mA $g^{-1}$.

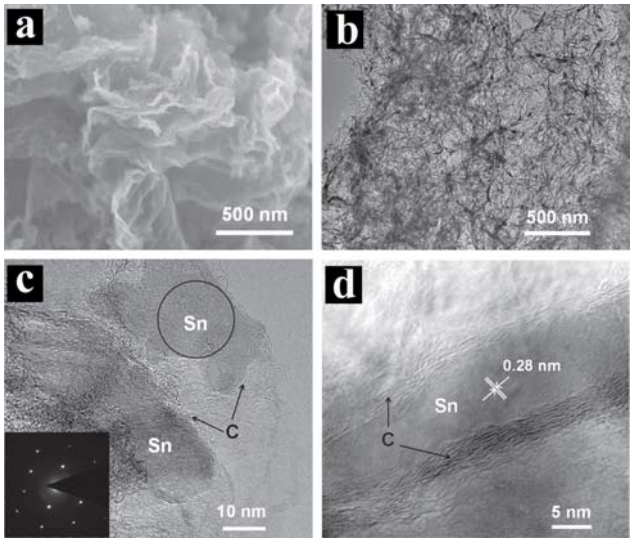


**Fig. 10** (a) SEM image of the GNS/Sn/GNS. (b) TEM image of the GNS/Sn/GNS. (c) TEM image showing Sn nanosheets and the inset image showing the SAED pattern of Sn nanosheets. (d) TEM image showing the cross-section of the sandwiched GNS/Sn/GNS. Reproduced with permission from ref. 190. Copyright Wiley 2012.

Chemical doping such as nitrogen doping is suggested as an effective way to improve the electrochemical properties of graphene and the supported Sn-based anodes.[61,199,200,224,226] Monodispersed ultrathin $SnO_2$ nanorods (2.5-4 nm in diameter and 10-15 nm in length) on nitrogen-doped GNS[224] is synthesized, as indicated in Fig. 11a-c. The initial discharge and charge capacities of 1996 and 1145 mAh $g^{-1}$ are observed for such a $SnO_2$/N-doped GNS composite at a current density of 100 mA $g^{-1}$. It also shows large reversible capabilities of 803 and 774 mAh $g^{-1}$ at current densities of 100 and 200 mA $g^{-1}$ after 100 cycles (Fig. 11d) and good high-rate performances (506 mAh $g^{-1}$ at a large current of 1000 mA $g^{-1}$ after 50 cycles with a small capacity loss of ~0.2% per cycle) due to the synergistic effect between $SnO_2$, GNS and nitrogen-doping. Nitrogen-doping is suggested to decrease the energy barrier for lithium ion penetrating, increase electrode/electrolyte wettability and generate more defects for lithium ion storage.[61,199,200,224,226]

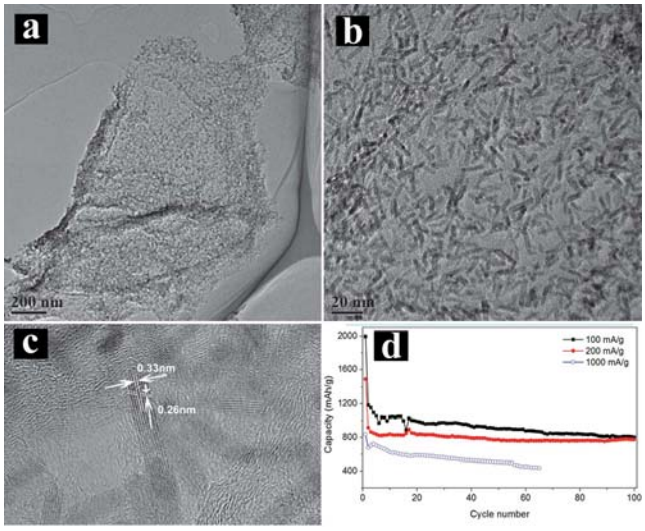


**Fig. 11** Ultrathin $SnO_2$ nanorods on N-doped GNS：(a-b) Low and high magnifications TEM images and (c) high-resolution TEM image of the ultrathin $SnO_2$ nanorods on GNS. (d) Cycling performance of $SnO_2$/GNS composite at current densities of 100, 200 and 1000 mA $g^{-1}$, respectively. Reproduced with permission from ref. 224. Copyright RSC 2012.

For Si-based electrodes, coating of carbon/graphene on the surface of nanostructured Si electrode[8,232] has been proved to be an efficient method to stabilize the interface between Si-based materials and electrolytes for the purpose of achieving a stable cycle life. But Si nanoparticle[233-260] structures are easier to be obtained in most of the graphene-supported Si-based anode reports. There are few reports dealing with GNS-supported Si nanowire[261-264] and thin film[265] structures.

Graphene layers are suggested to coat Si nanowires in Yang's article.[261] The active silicon nanowire (Si NW) consisting of silicon carbide nanocrystals (60-90 nm thickness of carbon layer), being surrounded by a uniform graphene shell, show outstanding large reversible capacity of 1650 mAh $g^{-1}$ after 500 charge-discharge cycles and extremely high Coulombic efficiencies of over 99% and 99.5% after 9 and 30 cycles, respectively. By the catalysis of gold, Si nanowires (20-50 nm in diameter) are in situ formed in a supercritical fluid-liquid-solid process as shown in Fig. 12.[262] The graphene supported Si nanowire exhibits an initial very large reversible lithium-extraction capacity of 2009 mAh $g^{-1}$ and a reversible capacity of 1400 mAh $g^{-1}$ are still observed after 30 cycles at 420 mA $g^{-1}$. Zhu and co-workers mix pre-formed silicon nanowires with graphene nanosheets by electrostatic self-assembly technique.[263] The nanowire-on-sheet composite exhibits reduced initial reversible capacity but improved cycling performances than previous report[261]. An initial reversible capacity of 1648 mAh $g^{-1}$ can be delivered, which remains 1335 mAh $g^{-1}$ after 80 cycles at 200 mA $g^{-1}$. More recently, graphene-supported Si nanowires are prepared by the catalysis of Au nanoparticles via a chemical vapor deposition route.[264] The composite shows a large initial reversible charge capacity of 2428 mAh $g^{-1}$ with a good capacity retention rate of 91.8% after 100 cycles at a current density of 300 mA $g^{-1}$. Compared to the aforementioned graphene-Sn based anodes, these graphene-Si based anodes generally have larger reversible capacities due to the larger theoretical value of Si element, but poorer cycling performances.

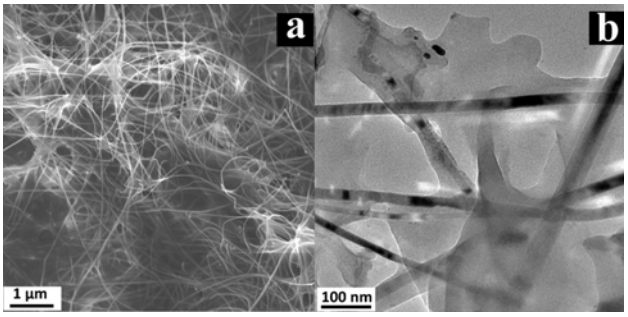


**Fig. 12** GNS-supported Si nanowires: (a) SEM image and (b) TEM image. Reproduced with permission from ref. 262. Copyright Elsevier 2013.

Germanium (Ge), an element of the same group of Sn and Si, also owns a high theoretical capacity of 1624 mAh $g^{-1}$. Recently, more research efforts have been paid to the GNS supported $Ge/GeO_2$ composites with different $Ge/GeO_2$ morphologies such as 0D $Ge/GeO_2$ nanoparticle[266-273] and 1D Ge nanowire[274,275].

Among graphene-supported $Ge/GeO_2$ nanoparticles, the further morphology modification of Ge or graphene structure can deliver improved Li-storage properties. Graphene supported Ge@C core-shell nanoparticles[270] exhibits excellent cycling performance (a reversible capacity of ~940 mAh $g^{-1}$ retained at a current density of 50 mA $g^{-1}$ after 50 cycles) and a good rate capability (380 mA h $g^{-1}$ retained at 3600 mA $g^{-1}$ after 50 cycles). 3D graphene scaffold supported Ge nanoparticles also exhibit excellent electrochemical performances (a reversible capacity of 1140 mAh $g^{-1}$ at 1/3C over 100 cycles and 835 mAh $g^{-1}$ at 8C after 60 cycles)[273].

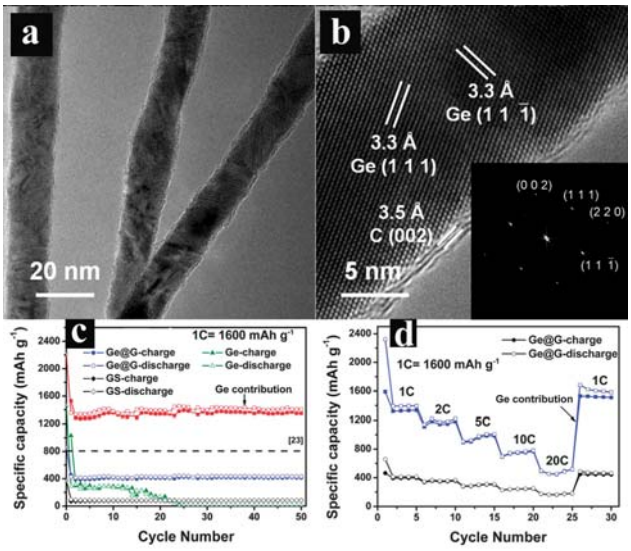


**Fig. 13** (a) TEM image of Ge@G. (b) HRTEM image of an individual Ge@G nanowire and its fast Fourier transform (FFT). (c) Cycling performance of the Ge@G. (d) Rate performance. Reproduced with permission from ref. 274. Copyright RSC 2013.

Graphene encapsulated 1D Ge nanowires, are sucessfully synthesized via a one-step arc-discharge route by Wang and his co-workers[274]. Ge nanowires (Fig. 13a and b) with 20 to 30 nanometers in diameter are encapsulated in graphene to form a Ge/graphene core-shell coaxial structure. The garphene-encapsulated Ge nanowire composite exhibits excellent electrochemical performance with a reversible capacity of 1400

mAh $g^{-1}$ (based on Ge contribution) after 50 cycles at a current density of 1600 mA $g^{-1}$ (Fig. 13c). The composite also exhibits excellent high-rate capability as shown in Fig. 13d. Another GNS/Ge nanowire composite is synthesized by growing graphene on the pre-synthesized individual Ge nanowires by a catalyst-free chemical vapor deposition (CVD) process.[275] The composite shows a highly reversible capacity of 1059 mAh $g^{-1}$ at a high C-rate (4.0 C) after 200 cycles. This capacity is corresponded to 90% of the initial reversible charge capacity.

## 4 Graphene-supported metal sulfides

Metal sulfides exhibit different lithium-ion storage mechanisms depending on the type of metal. In general, transitional metal sulfides such as $MoS_2$, CoS, NiS, CuS, FeS have large theoretical capacities because they are first reduced by lithium to transitional metal and lithium sulfide. The resultant lithium sulfide can decompose and be reproduced by reversible redox reactions. [38-40,43] In this regard, lithium sulfide exhibits similar function to lithium oxide obtained from lithium reduction of transitional metal oxide. However, main group metal sulfides such as $SnS_2$ and $In_2S_3$ exhibit a lithium-alloy mechanism.[41,44] For example, tin sulfide is reduced to tin and lithium sulfide. Tin can alloy and de-alloy reversibly with lithium ion to deliver a high capacity of 645 mAh $g^{-1}$, but the resultant lithium sulfide has similar inactive effect to lithium oxide obtained from lithium reduction of tin oxide. It should be noted that some metal sulfides such as $Sb_2S_3$ have been proposed to follow two types of lithium ion storage mechanisms induced by reversible decomposition of $Li_2S$ and Sb-Li alloying.[42]

### 4.1 Molybdenum sulfide

Molybdenum disulfide ($MoS_2$) is a layered transitional metal dichalcogenide compound composed of atom layers stacked together through van der Waals interactions.[38-40] The layered structure is helpful to allow lithium ions easily intercalate, therefore at the first stage of Li-ion storage (as described below), lithium ions intercalate into the S slab, leading to the breaking of the van der Waals S-S bonds and the formation of Li-S. Lithiated $MoS_2$ would then decompose into Mo nanoparticles, which are embedded in a $Li_2S$ matrix.

$$MoS_2 + xLi^+ + xe^- \rightarrow Li_xMoS_2$$

$$(4\text{-}x)Li^+ + Li_xMoS_2 + (4\text{-}x)e^- \leftrightarrow Mo + 2Li_2S$$

Due to its graphene-like layered structure, $MoS_2$ is inclined to form 2D sheet-like structure in the $MoS_2$-GNS nanocomposites.[276-290] The morphological and structural similarity between $MoS_2$ and GNS is the beneficial factor of property synergy. Therefore the sheet-on-sheet structure has received great interest as a promising electrode structure for LIBs. Among them, several examples of single-layer $MoS_2$-GNS composites have been obtained with commendable electrochemical properties[288-290].

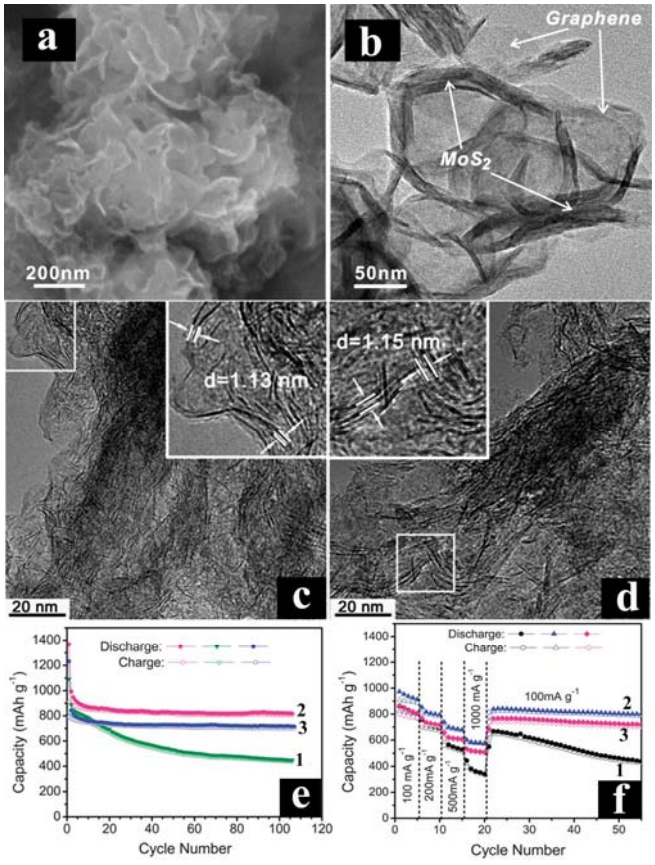


**Fig. 14** Microstructure of layered $MoS_2$/GNS (1:2) composite: (a) SEM image and (b) TEM image. Reproduced with permission from ref. 276. Copyright ACS 2011. TEM images of (c)single-layered $MoS_2$/GNS composite prepared from 0.02 M graphene oxide, denoted as $MoS_2$/GNS-02 and (d)Single-layered $MoS_2$/GNS composite prepared from 0.05 M graphene oxide, denoted as $MoS_2$/GNS-05. (e) Cycling performances and (f) Rate performances of (1) $MoS_2$, (2) $MoS_2$/GNS-02 , and (3) $MoS_2$/GNS-05. Reproduced with permission from ref. 290. Copyright RSC 2013.

$MoS_2$ nanosheet-graphene nanosheet hybrids are first prepared by Chen and co-workers by a hydrothermal technique.[276-277] The layered $MoS_2$ materials are tightly coupled with graphene nanosheets as shown in Fig. 14a and 14b. It is demonstrated that GNS could restrain the layered $MoS_2$ from well-stacking in the (002) plane, favoring the formation of few-layered $MoS_2$/GNS composites instead. A strong synergetic effect is observed in the sheet-on-sheet composite anodes. $MoS_2$-GNS (1:1), $MoS_2$-GNS (1:2), and $MoS_2$-GNS (1:4) composites exhibit charge capacities of 734, 1187, and 978 mAh $g^{-1}$ respectively after 100 cycles, which are substantially larger than the observed capacity of 256 mAh $g^{-1}$ for pristine $MoS_2$ after same cycle numbers. The composite also exhibits good rate capability, for example, at a large current of 1000 mA $g^{-1}$, a large reversible capacity of ~900 mAh $g^{-1}$ is maintained for the $MoS_2$-GNS (1:2). Recently, Chen and co-workers also report a similar GNS-supported single-layered $MoS_2$ structure[288,290] by the cationic surfactant assisted hydrothermal method (Fig. 14c-d). The single-layered $MoS_2$/GNS-02 composite (prepared from 0.02 M graphene oxide) exhibits a large reversible capacity of 808 mAh $g^{-1}$ at a small current of 100 mA $g^{-1}$ after 100 cycles with a small capacity loss of 1.04 mAh $g^{-1}$ per cycle. This reversible capacity

is larger than those of pristine $MoS_2$ (446 mAh $g^{-1}$) and $MoS_2$/GNS-05 composite (prepared from 0.05 M graphene oxide, 702 mAh $g^{-1}$) after same cycle numbers (Fig. 14e). Excellent high-rate performances are also observed for the single-layered $MoS_2$/GNS-02 composite (~600 mAh $g^{-1}$ at 1000 mA $g^{-1}$ as shown in Fig. 14f).[290] The microstructures and the electrochemical properties of graphene-like $MoS_2$/GNS for reversible lithium storage are dependent on the structure of the cationic surfactants and their concentrations in the hydrothermal solution.[290] Furthermore, the layer number of graphene-like $MoS_2$ nanosheets in the composites can also be controlled by using different cationic surfactants and their concentrations.[288]

Under the synergistic effect of a lithiation-assisted exfoliation process and a hydrazine monohydrate vapor reduction technique, $MoS_2$ nanosheet-graphene nanosheet hybrid is also fabricated.[278] The obtained nanosheets are in the range from several hundred nanometers to a few micrometers (Fig. 15). The $MoS_2$ nanosheet@GNS electrode achieves highly reversible large capacities. A reversible charge capacity of 915 mAh $g^{-1}$ can be retained after repetitive 700 cycles, while those of $MoS_2$ nanosheets and graphene are only 57 and 259 mAh $g^{-1}$ after 200 cycles, respectively. The high capacity, excellent rate capability, and long cycle life delivered in the above-mentioned $MoS_2$-GNS composite should be attributed to excellent structure affinity between $MoS_2$ nanosheets and GNS, which can facilitate the electron and lithium transportation, increase the contact area with electrolytes, and mechanical stability of the electrode.

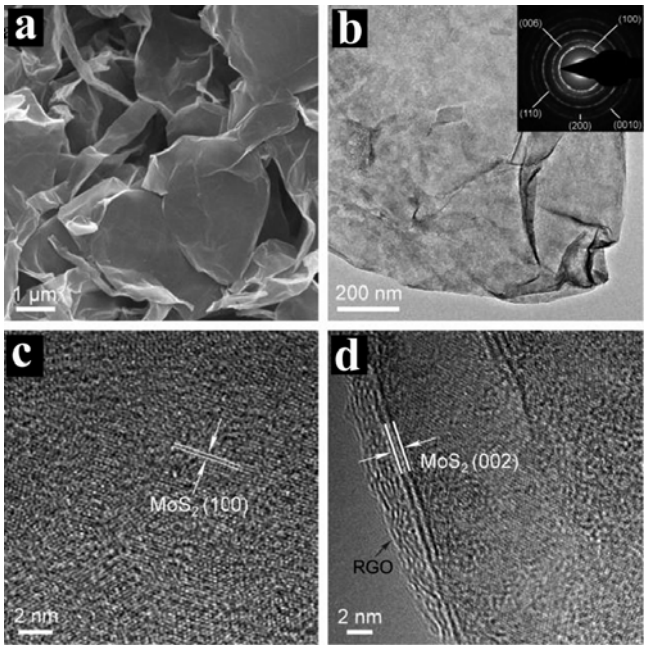


**Fig. 15** (a) SEM image of $MoS_2$ nanosheet-RGO. (b) TEM image of $MoS_2$ nanosheet-RGO, the inset shows the corresponding SAED pattern. (c) HRTEM image of the center of $MoS_2$ nanosheet-RGO. (d) HRTEM of the edge of $MoS_2$ nanosheet-RGO. Reproduced with permission from ref. 278. Copyright RSC 2013.

### 4.2 Tin sulfide

With a large theoretical capacity of 645 mAh $g^{-1}$, tin disulfide ($SnS_2$) is a promising anode for Li-ion batteries. Its lithium storage mechanism can be described as Sn-Li alloying/de-alloying process after $SnS_2$ reduction to Sn and $Li_2S$.[41] The formed $Li_2S$ intermediate cannot decompose reversibly and the active Li-ion storage element is only Sn. The storage mechanism of $SnS_2$ is very similar to that of $SnO_2$ with inactive elements of S and O.

$$SnS_2 + 4Li^+ + 4e^- \rightarrow Sn + 2Li_2S$$

$$Sn + xLi^+ + xe^- \leftrightarrow Li_xSn$$

Similar to Sn or $SnO_2$ anodes, the large volume change and electrode pulverization lead to the poor cycliabilities of $SnS_2$-based anodes, while the introduction of GNS to support tin sulfides have been proposed as an effective strategy to solve the problem. The reported $SnS_2$-GNS composites usually display two types of $SnS_2$ morphologies: nanoparticle-on-sheet[291-297] and nanosheet/nanoplate-on-sheet[298-304].

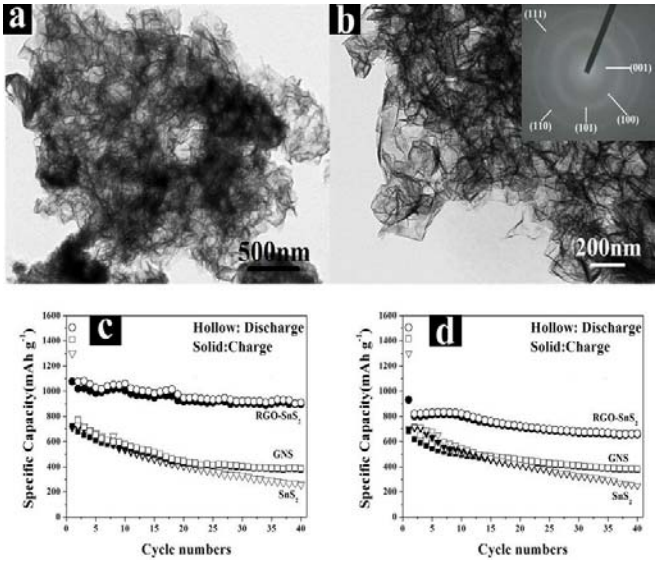


**Fig. 16** (a-b) TEM images of $SnS_2$-GNS sheet-on-sheet nanostructure, the inset SAED pattern of (b) showing polycrystalline $SnS_2$ structure. (c) Cycling performances at 0.1 C (66 mA $g^{-1}$). (d) Cycling performances at 1 C (660 mA $g^{-1}$). Reproduced with permission from ref. 299. Copyright ACS 2013.

With the assistance of fast microwave-assisted technique, a porous 3D $SnS_2$-GNS sheet-on-sheet nanostructure[299] has been synthesized recently, in which $SnS_2$ nanosheets are unfolded compared to pristine $SnS_2$ nanoflower and distributed uniformly on GNS surface (Fig. 16a and 16b). The cycling performance of the obtained graphene supported interconnected $SnS_2$ nanosheets at 0.1C and 1C are shown in Fig. 16c and 16d. It is clear that the $SnS_2$-GNS sheet-on-sheet composite achieves better electrochemical performances than bare graphene and pristine $SnS_2$ nanoflower. Large reversible capacities from 1077 to 896 mAh $g^{-1}$ and 934 to 657 mAh $g^{-1}$ are observed at 0.1 C and 1 C respectively during 40 cycles. The improved electrochemical properties have been largely ascribed to the closely-contacted

sheet-on-sheet composite, enabling the synergetic effect for highly reversible lithium ion storage.

Luo et al report a simple chemical vapor deposition, which is a facile approach to transform tin oxide nanoparticles into 2D $SnS_2$ nanoplates with different lateral sizes directly on/between graphene nanosheets.[301] The obtained 2D $SnS_2$@GNS sheet-on-sheet nanocomposite with different $SnS_2$ nanoplate sizes can be gained under different experimental conditions: high temperature pre-annealing of G-$SnO_2$ intermediate tends to form $SnS_2$ plates with small sizes (below 300 nm, Fig. 17b and 17c), while lower $H_2S$/Ar flow rate of CVD process can lead to $SnS_2$ plates with a larger size (Fig. 17d). The high reversible capacity of 668 mAh $g^{-1}$ after 10 cycles at a current of 100 mA $g^{-1}$ and excellent rate capability of 230 mAh $g^{-1}$ at a large current of 6400 mA $g^{-1}$ have been achieved for GNS-$SnS_2$-S anode with the smallest diameter (Fig. 17b).

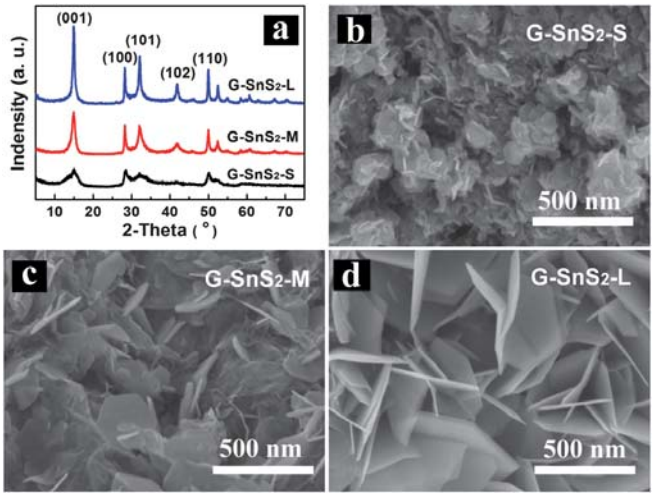


**Fig. 17** (a) XRD patterns and (b-d) SEM images of three typical graphene-$SnS_2$ samples with different lateral sizes of $SnS_2$ plates denoted as G-$SnS_2$-S/M/L. Reproduced with permission from ref. 301. Copyright RSC 2012.

### 4.3 Cobalt/nickel sulfide

Among various transitional metal sulfides, nickel sulfide has attracted a special interest for its abundant resource, less toxicity and high theoretical capacity (590 mAh $g^{-1}$), while cobalt sulfides with different stoichiometric ratios, such as CoS and $Co_3S_4$, have also shown great potential for use in LIBs, due to their high thermal stability and electrical conductivity.[305-309] The lithium storage mechanism of nickel sulfide and cobalt sulfide can be described as the following two-step reactions (1 and 2). The active Li-ion storage element is sulfur, which can store lithium basically based on the reversible formation and decomposition of $Li_2S$. The effect of $Li_2S$ is very similar to that of $Li_2O$ in previous Li-ion storage mechanism of transitional metal oxides. The overall reaction can be summarized by the reaction (3).

$$M_xS_y + nLi^+ + ne^- \leftrightarrow Li_nM_xS_y \quad (1)$$

$$(2y\text{-}n)\ Li^+ + Li_nM_xS_y + (2y\text{-}n)e^- \leftrightarrow x[M]^0 + yLi_2S \quad (2)$$

$$M_xS_y + 2ye^- + 2yLi^+ \leftrightarrow x[M]^0 + yLi_2S \quad (3)$$

As discussed above, the $Li_2S$ products are the intermediate in the Li-ion storage reactions for cobalt/nickel sulfides. The amorphous nature of graphene is helpful for absorbing the polysulfide anions, which prevents them from dissolution in the electrolyte. There are few reports on the GNS-supported cobalt/nickel sulfides, especially regarding the structure of 1D nanotube[305] or 2D nanosheet[306] embedded in GNS nanosheets. The outstanding lithium storage properties have been achieved in $CoS_x$-GNS nanoparticle-on-sheet composites with high reversible capacities reaching ~900 mAh $g^{-1}$ even after 50 charge-discharge cycles.[309] A NiS/GNS hybrid, that is synthesized by a facile one-pot hydrothermal method, exhibits ultrathin sheet-like NiS structure (below 5 nm) in the presence of graphene, forming a unique sheet-on-sheet nanostructure (Fig. 18a-b).[306] The unique ultrathin sheet structure of NiS and the combined conducting, buffering and confining effects of GNS are both beneficial for the rapid Li-ion transportation across the electrode/electrolyte interface. As a result, such NiS/GNS hybrid exhibits remarkably improved Li-storage properties compared to pristine NiS and a reversible capacity of 481 mAh $g^{-1}$ can be retained after 100 cycles with a good rate capability (386 mAh $g^{-1}$ at 800 mA $g^{-1}$) as indicated in Fig. 18c-d. Mahmood and co-workers report a novel GNS-supported $Co_3S_4$ nanotube[305] consisting of $Co_3S_4$ nanotubes with average diameter of 300 nm and lengths of a few microns on GNS. It shows a high discharge capacity of 720 mAh $g^{-1}$ up to 100 cycles with ~99.9% Columbic efficiencies.

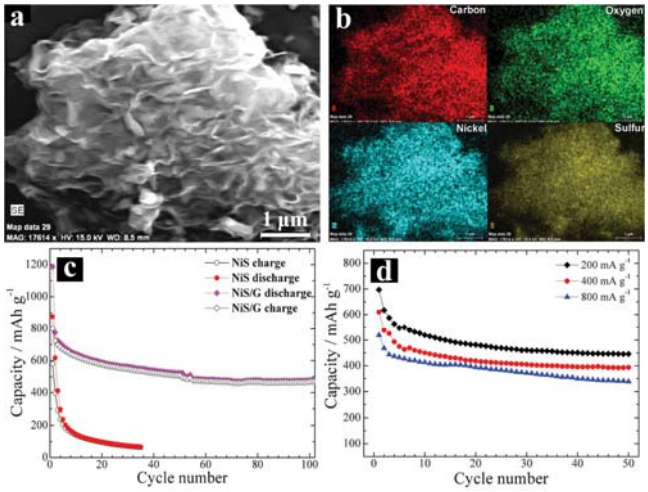


**Fig. 18** (a) SEM image and (b) EDS mapping of NiS nanosheet/GNS. (c) Cycling performances of NiS nanosheet/GNS and NiS at a current density of 50 mA $g^{-1}$. (d) Cycling performances of NiS nanosheet/GNS charged at large current densities of 200-800 mA $g^{-1}$ and discharged at 50 mA $g^{-1}$. Reproduced with permission from ref. 306. Copyright RSC 2013.

### 4.4 Other metal sulfides

In addition, some efforts have been devoted to graphene supported other main group metal sulfides (such as indium sulfide[44,310,311] and antimony sulfide[312]) and transitional metal sulfides (such as copper sulfide[313], iron sulfide[314], tungsten sulfide[315,316] and manganese sulfide[317]). The indium sulfides tend to form 2D nanosheet/plate morphologies with enhanced specific capacity and cycliability (the reversible capacities change from 1072 mAh $g^{-1}$ to 1015 mAh $g^{-1}$ after 100 cycles)[310] when embedded in GNS, while only antimony sulfide nanoparticles are

obtained on GNS[312], which can exhibit a reversible capacity of 720 mAh $g^{-1}$ after 50 cycles at a current density of 250 mA $g^{-1}$. It is worthy noting that two similar GNS-supported few-layered $WS_2$ nanosheet composites with different electrochemical properties are synthesized by hydrothermal reactions with[315] and without[316] a subsequent freeze-drying method. Besides, the GNS-MnS composite exhibits novel α-MnS hollow structure with porous shells embedded in the GNS nanosheet, which displays outstanding lithium storage properties.[317]

## 5 Graphene-carbon nanotube based composites

Recently, three dimensional Graphene-carbon nanotube composites[57,186-187,203-216,318-322] consisting of two dimensional graphene and one dimensional carbon nanotube (CNT), have attracted more research concerns. The 3D carbon-carbon composites can deliver synergistic effects between two different graphitic components with graphene layers being stabilized by aligned CNTs between the graphene nanosheets and the electrical conductivity along vertical direction of GNS being improved by bridging GNS vertically with CNTs. A physical mixture of GNS-CNT exhibits an increased reversible capacity of 730 mAh $g^{-1}$ compared to that of bare GNS (540 mAh $g^{-1}$).[57] As shown in Fig. 19, a series of GNS-CNT composites[318], marked by GNS-CNT-1, GNS-CNT-2 and GNS-CNT-3 are synthesized by chemical vapor reduction and deposition reactions performed at 500 °C for 2 min, 5 min and 1 h, respectively. The named "tip growth" mechanism is shown in Fig. 19a for the growth of CNTs on GNS. The corresponding HRTEM images of the products at different reaction stages are shown in Fig. 19b and confirm the growth mechanism of graphene-CNT nanocomposites. In such multilayered GNS-CNT composites, the tunable lengths of CNTs are achieved by adjusting the experimental conditions, which is a crucial factor for the electrochemical performances. The GNS-CNT-1 (Fig. 19c) with the shortest CNT length of 200-500 nm shows better electrochemical properties of a highly reversible capacity above 500 mAh $g^{-1}$ at both a small rate (0.2 C) and high rate (2 C) than the other GNS-CNT-2 (with the CNT length of 300-1500 nm, Fig. 19d) and GNS-CNT-3 (with the CNT length of 400-3000 nm, Fig. 19e) (Fig. 19f-g). This should be ascribed to the shortest length of CNTs in GNS-CNT-1, which can decrease the diffusion distance for lithium ions insertion and extraction. The improved properties of GNS-CNT compared to bare GNS (Fig. 19g) have been ascribed to the unique three dimensional conductive networks for efficient charge-transfer, increased electrical contact along both horizontal and vertical directions compared to bare graphene, and more active pores for Li-ions storage.[318]

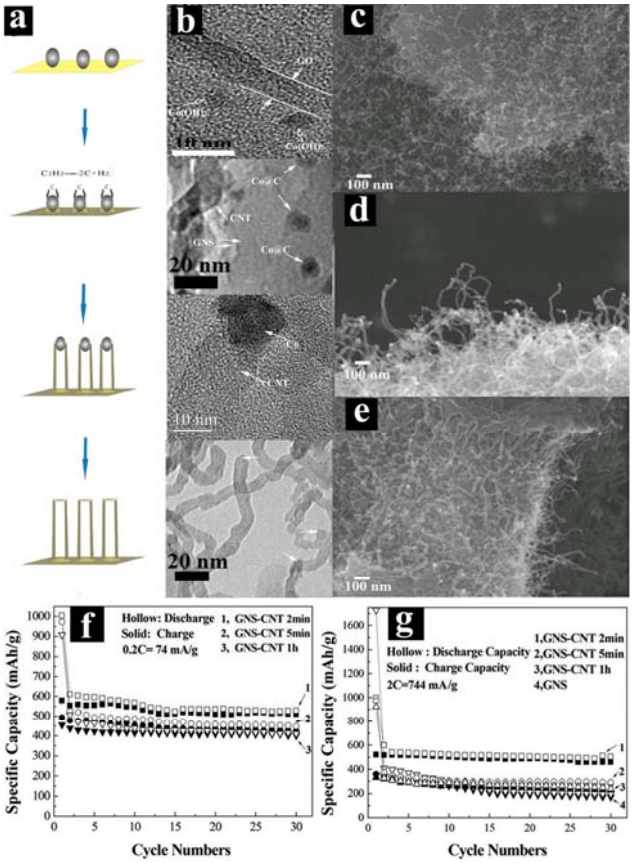


**Fig. 19** (a) Schematic illustration of the growth mechanism of graphene-CNT nanocomposite. (b) HRTEM images of GO-$Co(OH)_2$, Co@C, the Co-catalyzed CNT and CNTs in the composite (from the top to the bottom) corresponding to the left growth stages for CNT growth on GNS. SEM images of multilayered GNS-CNT composites with various growth times: (c) GNS-CNT-1, 2 min. (d) GNS-CNT-2, 5 min. (e) GNS-CNT-3, 1h. Cycling performances of the composites (f) at 74 mA $g^{-1}$ and (g) at 744 mA $g^{-1}$. Reproduced with permission from ref. 318. Copyright RSC 2011.

Another good example is 3D graphene-carbon nanotube-nickel (GNS-CNT-Ni) composite, synthesized by a cost-effective microwave-assisted method.[319] As shown in Fig. 20, well-packed forest of CNTs are grown uniformly on the GNS sheets by tailing the movement of the nickel nanoparticles. It should be noted that CNTs grow with various sizes of up to several nanometers in length and its diameter strongly depends on the particle size of nickel particles. These novel 3D GNS-CNT-Ni functional nanostructures show excellent performance (a reversible specific capacity of 648 mAh $g^{-1}$ after 50 cycles at a current density of 100 mA $g^{-1}$) due to the ultrahigh surface area, large number of activation sites and efficient ion diffusion. In comparison, CNT-Ni shows a smaller reversible capacity of 282 mAh $g^{-1}$ after 50 cycles. The high-rate cycling performances of GNS-CNT-Ni are also superior to those of CNT-Ni.

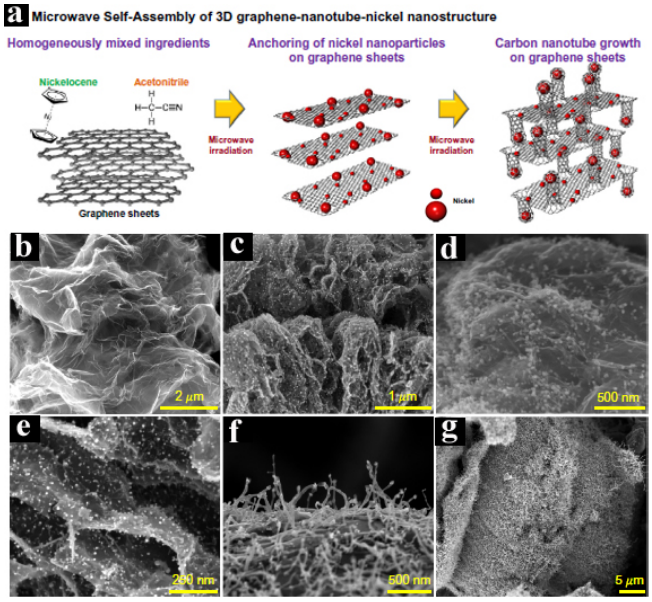


**Fig. 20** (a) Schematic of microwave-assisted synthesis of self-assembled 3D GNS-CNT-Ni nanostructure. SEM images of (b) a wavy reduced graphene oxide sheet obtained by thermal exfoliation, (c) uniformly decorated nickel nanoparticles on the graphene sheets, (d) initiation of CNT growth by nickel nanoparticles from the graphene surface, (e) well distributed nickel nanoparticles on the inner and outer surfaces of graphene, which induce CNT growth between graphene layers, (f) full-grown CNTs after completion of the microwave irradiation, and (g) CNTs densely grown over several graphene sheets, showing self-assembled 3D GNS-CNTs-Ni nanostructures. Reproduced with permission from ref. 319. Copyright Elsevier 2013.

Carbon nanotube and graphene nanosheets are both intriguing carbonaceous materials with unique properties including large surface areas, fast electronic conductivity, and flexible and robust microstructures. The combination of GNS and CNT materials may offer more intriguing properties. The synthesis of GNS-CNT composites also provides a new substrate to support[203,216,323-327] and even encapsulate[186-187] other high-capacity anode materials with the aim to improve their Li-ion storage properties. For example, a microwave irradiation technique is used to fabricate 3D GNS-CNT-$Fe_2O_3$ anode, which delivers a large reversible capacity of 1024 mAh $g^{-1}$ after 40 cycles along with a Coulombic efficiency approaching 100%.[325] The following merits are determined in these CNT-GNS composites: 1) The presence of GNS and CNTs can help each other to prevent the other one's aggregation, ensuring that unique properties of GNS and CNTs can be preserved for a long time for various applications. 2) Fast electronic conductivity of GNS is limited in the graphene layer and the presence of CNT can increase cross-plane conductivity by tightly coupled CNT with GNS. 3) Compared to bare GNS or CNT, the porous 3D GNS-CNT conductive network can further facilitate the electron and lithium transportation and electrolyte diffusion, and even store extra amounts of lithium ions in the porosity.

## 6 Perspectives and challenges

In summary, GNS-supported nanocomposites, which exhibit different morphologies and outstanding electrochemical properties, can be a good choice as the anode material for lithium ion batteries. A good control in the morphology and dimension of the GNS-based composite anodes is necessary since the electrochemical properties have been demonstrated to be highly dependent on the morphology, size, defect and composition in the composites. CuO is used as a typical example to represent the morphology-dependent Li-ion storage properties in presence of graphene. The following Table 2 compares the electrochemical performance of graphene-supported CuO composites with various 0D, 1D, 2D and 3D CuO morphologies. Based on similar experimental conditions such as test current and the weight percentage of graphene in the composites in our previous publicaions,[97-98] the CuO/GNS sheet-on-sheet composite[97] shows the largest reversible capacity compared to graphene supported fusiform[97]/shuttle[98]/urchin[98]-like CuO composites. A large reversible capacity of 801 mAh $g^{-1}$ is observed for the sheet-on-sheet composite after 40 cycles.[97] This reversible capacity is also larger than those of other graphene-supported composites such as

Table 2 Electrochemical properties of various graphene-supported CuO nanocomposites

| CuO morphology | Composite | Electrochemical Performances | Ref. |
|---|---|---|---|
| nanoparticle | CuO+GNS | A reversible capacity of 516 mAh $g^{-1}$ after 45 cycles at 0.1 mA $cm^{-2}$ (~525 mAh $g^{-1}$ after 40 cycles) and an initial discharge capacity of 1043 mAh $g^{-1}$ (the initial charge capacity is ~500 mAh $g^{-1}$) | 94 |
| nanoparticle | CuO+GNS | A reversible capacity of 441 mAh $g^{-1}$ after 50 cycles (~450 mAhg$^{-1}$ after 40 cycles) and an initial reversible charge capacity of 584 mAh $g^{-1}$ at a current density of 67 mA$g^{-1}$ | 95 |
| nanorod | CuO+GNS | A reversible capacity of 693 mA h $g^{-1}$ at 0.1 C rate and the discharge capacities are 936 and 606 mA h $g^{-1}$ respectively for the first and second cycles. | 96 |
| spindle | CuO+GNS | A reversible capacity of 666 mAh $g^{-1}$ after 40 cycles and an initial large charge capacity of ~ 956 mAh $g^{-1}$ at 70 mA $g^{-1}$ (0.1 C). | 97 |
| shuttle | CuO+GNS | A reversible capacity of 771 mAh $g^{-1}$ after 40 cycles and an initial large charge capacity of ~ 1243 mAh $g^{-1}$ at 70 mA $g^{-1}$ (0.1 C). | 98 |
| nanosheet | CuO+GNS | A reversible capacity of 801 mAh $g^{-1}$ after 40 cycles and an initial large charge capacity of ~ 1092 mAh $g^{-1}$ at 70 mA $g^{-1}$ (0.1 C). | 97 |
| nanosheet | CuO+GNS | A reversible capacity of ~737 mAh $g^{-1}$ after 50 cycles (~750 mAh $g^{-1}$ after 40 cycles) and an initial charge capacity of ~ 800 mAh $g^{-1}$ at 0.1 C (67 mA $g^{-1}$). | 99 |
| flower | CuO+GNS | A reversible capacity of ~590 mAh $g^{-1}$ after 40 cycles and an initial charge capacity of ~ 603 mAh $g^{-1}$ at 0.1 C (67 mA $g^{-1}$). | 100 |
| urchin | CuO+GNS | A reversible capacity of ~634 mAh $g^{-1}$ after 40 cycles and an initial charge capacity of ~ 999 mAh $g^{-1}$ at 0.1 C (70 mA $g^{-1}$). | 98 |
| urchin | CuO+GNS | A reversible capacity of ~600 mAh $g^{-1}$ after 40 cycles, and an initial charge capacity of ~ 620 mAh $g^{-1}$ at 65 mA $g^{-1}$. | 101 |

0D CuO nanoparticles[94-95], 1D nanorod[96] and 3D nanoflower[100]/ urchin[101] after same cycle numbers (such comparison can only be regarded as rough estimation because the experimental conditions such as test currents and the composite composition are not same). Among these various CuO morphologies indicated in Table 2, graphene supported 0D CuO nanoparticles generally display the lowest reversible capacities (440-580 mAh $g^{-1}$)[94-95] compared to graphene supported 1D, 2D and 3D CuO morphologies.

In general, GNS supported 1D, 2D, and 3D electrode structures exhibit more attractive properties than 0D nanoparticles under similiar experimental conditions. From the viewpoint of contact efficiency between graphene and the supported materials, the structure affinity of two components should be the most important. GNS substrate is a 2D nanosheet structure and the introduced second-phase supported materials should be 2D as well to fit GNS well. Such a surface-to-surface contact is the best model for structure affinity between GNS and the introduced supported materials. In contrast, the contact between 2D GNS and 1D/0D supported materials is in line-to-line or point-to-point mode, which has less contact area. Moreover, the supported 3D structure also has less contact area with graphene because usually only one face of the 3D structure is contacted with graphene. In this regard, GNS-supported sheet-on-sheet structure is believed to be a perfect composite structure to achieve outstanding synergetic electrochemical performance, mainly attributed to the synergic effect of the supported nanosheet structure and GNS with same dimensionality (Scheme 1). The 2D structure of the supported materials can be contacted tightly with 2D GNS materials according to a large surface contact area compared with 3D structure, 1D nanowire/nanorod/nanotube and 0D nanoparticle. Therefore the electrical conductivity and mechanical stability of 2D nanosheets can be improved by GNS upon repetitive cycling, and GNS can be better separated against restacking into graphite platelets, which would lose its promising properties relative to unique few-layer structure. Moreover, 0D nanoparticles would tend to be agglomerated due to a small particle size upon repetitive cycling despite the presence of GNS. The agglomerated big particle may be pulverized and lose the electrical contact with current collector under inhomogeneous mechanical stress induced by large volume change during lithium insertions (Scheme 1).

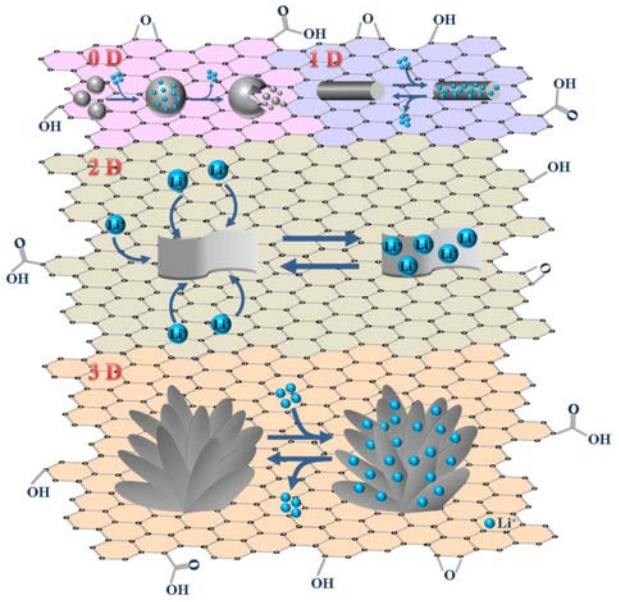


**Scheme 1** Schematic illustration showing lithium storage in graphene supported 0D, 1D, 2D and 3D electrode nanostructures.

The choice and modification of graphene and its derivatives with different surface characteristics and microstructures are essential to the resultant graphene-supported composites and their Li-ion storage properties.[328] Graphene oxides (GO) and reduced graphene oxides (RGO) powders are often used as the start materials in the current synthesis approaches for various GNS-based composites. The GO is prepared by chemical oxidation using strong oxidation agents. There are abundant surface groups such as hydroxyl, carboxyl, and epoxy groups. The reduced GO still remains a small amount of these oxygen-functionalized groups. These surface groups have significant effects in the solution-based preparation of GNS-supported composites. Therefore the product morphology can be tuned by using whether GO or RGO with various reduction extents and varying the usage amount of RGO,[40,44,115] besides other experimental conditions such as the reaction solvent, temperature, and structure-directing agent. Moreover, the binding effect between graphene and the supported materials is largely affected by these surface groups/functionalities, which should be a crucial factor to the structure stability of the GNS-supported composites when used for repeated cycling with lithium ions. The possible linkages such as metal-O-, S-H-, have been proposed in graphene-supported metal oxides and metal sulfides.[28,70,88,96,276-278,290] Chemical doping with other elements such as nitrogen[61,199,200,224,226,329] and boron[329-330] has also been used to modify graphene structure and achieved significantly improved electrochemical properties for graphene-based composites anodes. It is found that the nitrogen-doping can greatly generate more defects for large capacity for lithium ion storage and decrease the energy barrier for lithium-ion intercalation and de-intercalation and boron doped graphene can store more lithium ions in the resultant electron-deficient system[330]. Porous activated graphene nanosheet by carbon dioxide or KOH activation is also a promising technique, which can deliver further open pore structure in the planar sheet with increased surface areas.[214,331]

Besides being powders in most reports, graphene or reduced graphene oxide nanosheets have been recently prepared in other macroscopical states with intriguing electrochemical properties. For example, the 3D graphene aerogels (GAS) [332-333] and the crumpled 3D sphere by self-assembly of graphene[123] developed recently have been proved to own high specific surface area and percolated network, which can transport and store charge with very low bulk density. Graphene aerogels are simple and intriguing matrix to be composited with metal/metal oxide-based active anode materials,[201,334] and GAS-involved nanocomposites exhibit enhanced electrical conductivity and facilitated lithium and electrolyte diffusion when used as high-surface-area electrodes for lithium ion battery. Moreover, 2D graphene-based composite film prepared by vacuum infiltration of the graphene-

based dispersion[335-337,84,89,118] or CVD growth on catalytic metal substrate[338-341], as advanced electrode materials, have attracted more and more attentions due to their improved mechanical stability, fast electron-transfer kinetics and excellent electrochemical activity without the need of binder and additional conducting agents. Lastly, 1D graphene nanoribbons derived from 1D CNT have been explored for Li-ion batteries.[196,342] These 3D, 2D and 1D GNS-based composites can transfer the intrinsic features of the individual components and may attract more research concerns in a near future.

Although attractive results have been achieved for GNS-supported various nanocomposites as electrode materials for LIBs, there are still some existing challenges or drawbacks, which need to be conquered in the future: (1) The fundamental lithium storage mechanism in graphene-based composites is yet to be fully understood especially with respects to their surface functionalities/defects and hierarchical electrode structures. (2) The voltage plateau of graphene-based composites are usually not flat because most graphene in the composites are largely disordered carbon for the purpose of large Li-ion storage capacity and fast and easy lithium intercalation. Some graphene-supported composites such as transitional metal oxides and metal sulfides have a comparatively high voltage range for lithium insertion and extraction. These issues would affect the stable output of the energy and reduce the power density of the battery. (3) The high cost of GNS-based electrode materials significantly restrict their scalable production and application. The high surface area of graphene and its composites may lead to the large irreversible capacity loss in the first cycle and the porosity in the graphene-based composite exhibit a small tap density and subsequently an unfavorable low volumetric capacity.

It is believed that more efforts should be focused on the control of morphology, porosity, size, defects, alignment of the graphene-based composites and understanding the interfacial interactions between graphene and the introduced second-phase functional compounds to achieve better electrochemical performance. Graphene-based electrode materials for LIBs will realize more practical applications such as personal electronics, electric vehicles, hybrid electric vehicles, and scalable energy storage.

**Acknowledgements** The authors gratefully acknowledge the follow-up Program for Professor of Special Appointment in Shanghai (Eastern Scholar), the National Natural Science Foundation of China (51271105 and 51201095), Shanghai Municipal Government (13YZ012, 11JC1403900, 11SG38) and Innovative Research Team (IRT13078) for financial support.

Notes and references

[a] *Department of Chemical Engineering, School of Environmental and Chemical Engineering, Shanghai University, Shangda Road 99, Shanghai, 200444, P. R. China. Fax:+86-21-66137725; Tel: +86-21-66137723; E-mail: yongwang@ shu.edu.cn*

1 B. Scrosati and J. Garche, *J. Power Sources*, 2010, **195**, 2419-2430.
2 V. Etacheri, R. Marom, R. Elazari, G. Salitra and D. Aurbach, *Energy Environ. Sci.*, 2011, **4**, 3243-3262.
3 P. G. Bruce, B. Scrosati and J. M. Tarascon, *Angew. Chem. Int. Ed.*, 2008, **47**, 2930-2946.
4 G. M. Zhou, F. Li and H. M. Cheng, *Energy Environ. Sci.*, 2014, **7**, 1307-1338.
5 L. W. Su, Y. Jing and Z. Zhou, *Nanoscale*, 2011, **3**, 3967-3983.
6 B. Wang, B. Luo, X. L. Li and L. J. Zhi, *Mater. Today*, 2012, **15**, 544-552.
7 H. S. Im, Y. J. Cho, Y. R. Lim, C. S. Jung, D. M. Jang, J. Park, F. Shojaei and H. S. Kang, *ACS Nano*, 2013, **7**, 11103-11111.
8 X. L. Wu, Y. G. Guo and L. J. Wan, *Chem. Asian J.*, 2013, **8**, 1948-1958.
9 J. L. Gómez-Cámer, C. Villevieille and P. Novák, *J. Mater. Chem. A*, 2013, **1**, 13011-13016.
10 P. Chen, F. D. Wu and Y. Wang, *ChemSusChem*, 2014, **7**, 1407-1414.
11 Y. Gu, F. D. Wu and Y. Wang, *Adv. Funct. Mater.*, 2013, **23**, 893-899.
12 Y. Wang, M. H. Wu, Z. Jiao and J. Y. Lee, *Chem. Mater.*, 2009, **21**, 3210-3215.
13 J. S. Chen and X. W. Lou, *small*, 2013, **9**, 1877-1893.
14 P. Poizot, S. Laruelle, S. Grugeon, L. Dupont and J. M. Tarascon, *Nature*, 2000, **407**, 496-499.
15 J. Cabana, L. Monconduit, D. Larcher and M. R. Palacin, *Adv. Mater.*, 2010, **22**, E170-E192.
16 J. Jiang, Y. Y. Li, J. P. Liu and X. T. Huang, *Nanoscale*, 2011, **3**, 45-58.
17 Y. Y. Mai, F. Zhang and X. L. Feng, *Nanoscale*, 2014, **6**, 106-121.
18 H. B. Wu, J. S. Chen, H. H. Hng and X. W. Lou, *Nanoscale*, 2012, **4**, 2526-2542.
19 W. Wei, Z. H. Wang, Z. Liu, Y. Liu, L. He, D. Z. Chen, A. Umar, L. Guo and J. H. Li, *J. Power Sources*, 2013, **238**, 376-387.
20 M. V. Reddy, G. V. S. Rao and B. V. R. Chowdari, *Chem. Rev.*, 2013, **113**, 5364-5457.
21 Y. Lu, Y. Wang, Y. Q. Zou, Z. Jiao, B. Zhao, Y. Q. He and M. H. Wu, *Electrochem. Commun.*, 2010, **12**, 101-105.
22 F. D. Wu, M. H. Wu and Y. Wang, *Electrochem. Commun.*, 2011, **13**, 433-436.
23 F. D. Wu and Y. Wang, *J. Mater. Chem.*, 2011, **21**, 6636-6641.
24 Y. Q. Zou and Y. Wang, *Chem. Eng. J.*, 2013, **229**,183-189.
25 W. J. Lee, M. H. Park, Y. Wang, J. Y. Lee and J. Cho, *Chem. Commun.*, 2010, **46**, 622-624.
26 Y. Wang, M. .H. Wu, Z. Jiao and J. Y. Lee, *Nanotechnology*, 2009, **20**, 345704.
27 Z. C. Bai, Z. C. Ju, C. L. Guo, Y. T. Qian, B. Tang and S. L. Xiong, *Nanoscale*, 2014, **6**, 3268-3273.
28 Z. S. Wu, G. M. Zhou, L. C. Yin, W. C. Ren, F. Li and H. M. Cheng, *Nano Energy*, 2012, **1**, 107-131.
29 D. W. Kim, I. S. Hwang, S. J. Kwon, H. Y. Kang, K. S. Park, Y. J. Choi, K. J. Choi and J. G. Park, *Nano Lett.*, 2007, **7**, 3041-3045.
30 S. Chen, M. Wang, J. F. Ye, J. G. Cai, Y. R. Ma, H. H. Zhou and L. M. Qi, *Nano Res.*, 2013, **6**, 243-252.
31 R. Yang, J. Zheng, J. Huang, X. Z. Zhang, J. L. Qu and X. G. Li, *Electrochem. Commun.*, 2010, **12**, 784-787.
32 D. D. Li, L. X. Ding, S. Q. Wang, D. D. Cai and H. H. Wang, *J. Mater. Chem. A*, 2014, **2**, 5625-5630.
33 S. Y. Gao, S. X. Yang, J. Shu, S. X. Zhang, Z. D. Li and K. Jiang, *J. Phys. Chem. C*, 2008, **112**, 19324-19328.
34 J. Y. Xiang, J. P. Tu, L. Zhang, Y. Zhou, X. L.Wang and S. J. Shi, *J. Power Sources*, 2010, **195**, 313-319.
35 X. D. Xu, R. G. Cao, S. Jeong and J. Cho, *Nano Lett.*, 2012, **12**, 4988-4991.
36 Y. M. Lin, P. R. Abel, A. Heller and C. B. Mullins, *J. Phys. Chem. Lett.*, 2011, **2**, 2885-2891.
37 B. Sun, J. Horvat, H. S. Kim, W. S. Kim, J. Ahn and G. X. Wang, *J. Phys. Chem. C*, 2010, **114**, 18753-18761.
38 T. Stephenson, Z. Li, B. Olsen and D. Mitlin, *Energy Environ. Sci.*, 2014, **7**, 209-231.
39 T. Yang, Y. J. Chen, B. H. Qu, L. Mei, D. N. Lei, H. N. Zhang, Q. H. Li and T. H. Wang, *Electrochim. Acta*, 2014, **115**, 165-169.
40 M. Wang, G. D. Li, H. Y. Xu, Y. T. Qian and J. Yang, *ACS Appl. Mater. Interfaces*, 2013, **5**, 1003-1008.
41 Y. P. Du, Z. Y. Yin, X. H. Rui, Z. Y. Zeng, X. J. Wu, J. Q. Liu, Y. Y. Zhu, J. X. Zhu, X. Huang, Q. Y. Yan and H. Zhang, *Nanoscale*, 2013, **5**, 1456-1459.

42 P. V. Prikhodchenko, J. Gun, S. Sladkevich, A. A. Mikhaylov, O. Lev, Y. Y. Tay, S. K. Batabyal and D. Y. W. Yu, *Chem. Mater.*, 2012, **24**, 4750-4757.

43 Q. H. Wang, L. F. Jiao, H. M. Du, W. X. Peng, Y. Han, D. W. Song, Y. C. Si, Y. J. Wang and H. T. Yuan, *J. Mater. Chem.*, 2011, **21**, 327-329.

44 Y. Gu and Y. Wang, *RSC Adv.*, 2014, **4**, 8582-8589.

45 D. Janas and K. K. Koziol, *Nanoscale*, 2014, **6**, 3037-3045.

46 S. Xin, Y. G. Guo and L. J. Wan, *Acc. Chem. Res.*, 2012, **45**, 1759-1769.

47 D. P. Upare, S. Yoon and C. W. Lee, *Korean J. Chem. Eng.*, 2011, **28**, 731-743.

48 B. J. Landi, M. J. Ganter, C. D. Cress, R. A. DiLeo and R. P. Raffaelle, *Energy Environ. Sci.*, 2009, **2**, 638-654.

49 X. M. Liu, Z. D. Huang, S. W. Oh, B. Zhang, P. C. Ma, M. M. F. Yuen and J. K. Kim, *Compos. Sci. Technol.*, 2012, **72**, 121-144.

50 K. S. Novoselov, A. K. Geim, S. V. Morozov, D. Jiang, Y. Zhang, S. V. Dubonos, I. V. Grigorieva and A. A. Firsov, *Science*, 2004, **306**, 666-669.

51 S. B. Yang, X. L. Feng, L. Wang, K. Tang, J. Maier and K. Müllen, *Angew. Chem. Int. Ed.*, 2010, **49**, 4795-4799.

52 K. S. Novoselov, V. I. Fal'ko, L. Colombo, P. R. Gellert, M. G. Schwab and K. Kim, *Natrue*, 2012, **490**, 192-200.

53 A. K. Geim and K. S. Novoselov, *Nat. Mater.*, 2007, **6**, 183-191.

54 M. J. Allen, V. C. Tung and R. B. Kaner, *Chem. Rev.*, 2010, **110**, 132-145.

55 C. N. R. Rao, A. K. Sood, K. S. Subrahmanyam and A. Govindaraj, *Angew. Chem. Int. Ed.*, 2009, **48**, 7752-7777.

56 V. Chabot, D. Higgins, A. P. Yu, X. C. Xiao, Z. W. Chen and J. J. Zhang, *Energy Environ. Sci.*, 2014, **7**, 1564-1596.

57 E. Yoo, J. Kim, E. Hosono, H. S. Zhou, T. Kudo and I. Honma, *Nano Lett.*, 2008, **8**, 2277-2282.

58 G. X. Wang, X. P. Shen, J. Yao and J. Park, *Carbon*, 2009, **47**, 2049-2053.

59 P. C. Lian, X. F. Zhu, S. Z. Liang, Z. Li, W. S. Yang and H. H. Wang, *Electrochim. Acta*, 2010, **55**, 3909-3914.

60 D. Y. Pan, S. Wang, B. Zhao, M. H. Wu, H. J. Zhang, Y. Wang and Z. Jiao, *Chem. Mater.*, 2009, **21**, 3136-3142.

61 A. L. M. Reddy, A. Srivastava, S. R. Gowda, H. Gullapalli, M. Dubey and P. M. Ajayan, *ACS Nano*, 2010, **4**, 6337-6342.

62 X. Huang, Z. Y. Zeng, Z. X. Fan, J. Q. Liu and H. Zhang, *Adv. Mater.*, 2012, **24**, 5979-6004.

63 M. H. Liang and L. J. Zhi, *J. Mater. Chem.*, 2009, **19**, 5871-5878.

64 D. H. Lee, J. C. Kim, H. W. Shim and D. W. Kim, *ACS Appl. Mater. Interfaces*, 2014, **6**, 137-142.

65 I. R. M. Kottegoda, N. H. Idris, L. Lu, J. Z. Wang and H. K. Liu, *Electrochim. Acta*, 2011, **56**, 5815-5822.

66 X. J. Zhu, J. Hu, H. L. Dai, L. Ding and L. Jiang, *Electrochim. Acta*, 2012, **64**, 23-28.

67 S. G. Hwang, G. O. Kim, S. R. Yun and K. S. Ryu, *Electrochim. Acta*, 2012, **78**, 406-411.

68 Y. Q. Zou and Y. Wang, *Nanoscale*, 2011, **3**, 2615-2620.

69 J. T. Zai, C. Yu, L. Q. Tao, M. Xu, Y. L. Xiao, B. Li, Q. Y. Han, K. X. Wang and X. F. Qian, *CrystEngComm*, 2013, **15**, 6663-6671.

70 G. M. Zhou, D. W. Wang, L. C. Yin, N. Li, F. Li and H. M. Cheng, *ACS Nano*, 2012, **6**, 3214-3223.

71 Y. J. Mai, S. J. Shi, D. Zhang, Y. Lu, C. D. Gu and J. P. Tu, *J. Power Sources*, 2012, **204**, 155-161.

72 Y. Huang, X. L. Huang, J. S. Lian, D. Xu, L. M. Wang and X. B. Zhang, *J. Mater. Chem.*, 2012, **22**, 2844-2847.

73 D. F. Qiu, Z. J. Xu, M. B. Zheng, B. Zhao, L. J. Pan, L. Pu and Y. Shi, *J. Solid State Electrochem.*, 2012, **16**, 1889-1892.

74 D. Xie, Q. M. Su, W. W. Yuan, Z. M. Dong, J. Zhang and G. H. Du, *J. Phys. Chem. C*, 2013, **117**, 24121-24128.

75 L. Q. Tao, J. T. Zai, K. X. Wang, Y. H. Wan, H. J. Zhang, C. Yu, Y. L. Xiao and X. F. Qian, *RSC Adv.*, 2012, **2**, 3410-3415.

76 L. Y. Pan, H. B. Zhao, W. C. Shen, X. W. Dong and J. Q. Xu, *J. Mater. Chem. A*, 2013, **1**, 7159-7166.

77 B. J. Li, H. Q. Cao, J. Shao, G. Q. Li, M. Z. Qu and G. Yin, *Inorg. Chem.*, 2011, **50**, 1628-1632.

78 H. Kim, D. H. Seo, S. W. Kim, J. Kim and K. Kang, *Carbon*, 2011, **49**, 326-332.

79 Z. S. Wu, W. C. Ren, L. Wen, L. B. Gao, J. P. Zhao, Z. P. Chen, G. M. Zhou, F. Li and H. M. Cheng, *ACS Nano*, 2010, **4**, 3187-3194.

80 B. G. Choi, S. J. Chang, Y. B. Lee, J. S. Bae, H. J. Kim and Y. S. Huh, *Nanoscale*, 2012, **4**, 5924-5930.

81 X. L. Yang, K. C. Fan, Y. H. Zhu, J. H. Shen, X. Jiang, P. Zhao and C. Z. Li, *J. Mater. Chem.*, 2012, **22**, 17278-17283.

82 Y. Qi, H. Zhang, N. Du and D. R. Yang, *J. Mater. Chem. A*, 2013, **1**, 2337-2342.

83 W. B. Yue, Z. Z. Lin, S. H. Jiang and X. J. Yang, *J. Mater. Chem.*, 2012, **22**, 16318-16323.

84 X. L. Yang, K. C. Fan, Y. H. Zhu, J. H. Shen, X. Jiang, P. Zhao, S. R. Luan and C. Z. Li, *ACS Appl. Mater. Interfaces*, 2013, **5**, 997-1002.

85 Q. Wang, C. Y. Zhang, X. B. Xia, L. L. Xing and X. Y. Xue, *Mater. Lett.*, 2013, **112**, 162-164.

86 Z. Zhang, J. H. Hao, W. S. Yang, B. P. Lu, X. Ke, B. L. Zhang and J. L. Tang, *ACS Appl. Mater. Interfaces*, 2013, **5**, 3809-3815.

87 L. Q. Tao, J. T. Zai, K. X. Wang, H. J. Zhang, M. Xu, J. Shen, Y. Z. Su and X. F. Qian, *J. Power Sources*, 2012, **202**, 230-235.

88 S. Q. Chen and Y. Wang, *J. Mater. Chem.*, 2010, **20**, 9735-9739.

89 R. H. Wang, C. H. Xu, J. Sun, Y. Q. Liu, L. Gao and C. C. Lin, *Nanoscale*, 2013, **5**, 6960-6967.

90 L. Wang, D. L. Wang, J. S. Zhu and X. S. Liang, *Ionics*, 2013, **19**, 215-220.

91 G. P. Kim, I. Nam, N. D. Kim, J. Park, S. Park and J. Yi, *Electrochem. Commun.*, 2012, **22**, 93-96.

92 W. Y. Zhang, Y. Zeng, N. Xiao, H. H. Hng and Q. Y. Yan, *J. Mater. Chem.*, 2012, **22**, 8455-8461.

93 J. S. Zhou, L. L. Ma, H. H. Song, B. Wu and X. H. Chen, *Electrochem. Commun.*, 2011, **13**, 1357-1360.

94 A. K. Rai, L. T. Anh, J. Gim, V. Mathew, J. Kang, B. J. Paul, N. K. Singh, J. J. Song and J. Kim, *J. Power Sources*, 2013, **244**, 435-441.

95 Y. J. Mai, X. L. Wang, J. Y. Xiang, Y. Q. Qiao, D. Zhang, C. D. Gu and J. P. Tu, *Electrochim. Acta*, 2011, **56**, 2306-2311.

96 Q. Wang, J. Zhao, W. F. Shan, X. B. Xia, L. L. Xing and X. Y. Xue, *J. Alloys Compd.*, 2014, **590**, 424-427.

97 L. Q. Lu and Y. Wang, *J. Mater. Chem.*, 2011, **21**, 17916-17921.

98 L. Q. Lu and Y. Wang, *Electrochem. Commun.*, 2012, **14**, 82-85.

99 Y. Liu, W. Wang, L. Gu, Y. W. Wang, Y. L. Ying, Y. Y. Mao, L. W. Sun and X. S. Peng, *ACS Appl. Mater. Interfaces*, 2013, **5**, 9850-9855.

100 H. Cheng, F. Feng, Z. L. Hu, F. S. Liu, W. Q. Gong and K. X. Xiang, *Trans. Nonferrous Met. Soc. China*, 2012, **22**, 2523-2528.

101 B. Wang, X. L. Wu, C. Y. Shu, Y. G. Guo and C. R. Wang, *J. Mater. Chem.*, 2010, **20**, 10661-10664.

102 X. J. Zhu, Y. W. Zhu, S. Murali, M. D. Stoller and R. S. Ruoff, *ACS Nano*, 2011, **5**, 3333-3338.

103 L. Xiao, D. Q. Wu, S. Han, Y. S. Huang, S. Li, M. Z. He, F. Zhang and X. L. Feng, *ACS Appl. Mater. Interfaces*, 2013, **5**, 3764-3769.

104 J. X. Zhu, T. Zhu, X. Z. Zhou, Y. Y. Zhang, X. W. Lou, X. D. Chen, H. Zhang, H. H. Hng and Q. Y. Yan, *Nanoscale*, 2011, **3**, 1084-1089.

105 G. W. Zhou, J. L. Wang, P. F. Gao, X. W. Yang, Y. S. He, X. Z. Liao, J. Yang and Z. F. Ma, *Ind. Eng. Chem. Res.*, 2013, **52**, 1197-1204.

106 M. Zhang, B. H. Qu, D. N. Lei, Y. J. Chen, X. Z. Yu, L. B. Chen, Q. H. Li, Y. G. Wang and T. H. Wang, *J. Mater. Chem.*, 2012, **22**, 3868-3874.

107 L. L. Tian, Q. C. Zhuang, J. Li, C. Wu, Y. L. Shi and S. G. Sun, *Electrochim. Acta*, 2012, **65**, 153-158.

108 Z. L. Jian, B. Zhao, P. Liu, F. J. Li, M. B. Zheng, M. W. Chen, Y. Shi and H. S. Zhou, *Chem. Commun.*, 2014, **50**, 1215-1217.

109 M. Du, C. H. Xu, J. Sun and L. Gao, *J. Mater. Chem. A*, 2013, **1**, 7154-7158.

110 Y. Q. Zou, J. Kan and Y. Wang, *J. Phys. Chem. C*, 2011, **115**, 20747-20753.

111 W. F. Chen, S. R. Li, C. H. Chen and L. F. Yan, *Adv. Mater.*, 2011, **23**, 5679-5683.

112 X. D. Huang, B. Sun, S. Q. Chen and G. X. Wang, *Chem. Asian J.*, 2014, **9**, 206-211.

113 W. Wei, S. B. Yang, H. X. Zhou, I. Lieberwirth, X. L. Feng and K. Müllen, *Adv. Mater.*, 2013, **25**, 2909-2914.

114 J. Z. Wang, C. Zhong, D. Wexler, N. H. Idris, Z. X. Wang, L. Q. Chen and H. K. Liu, *Chem. Eur. J.*, 2011, **17**, 661-667.

115 J. Kan and Y. Wang, *Sci. Rep.*, 2013, **3**, 3502-3511.

116 X. Y. Xue, C. H. Ma, C. X. Cui and L. L. Xing, *Solid State Sci.*, 2011, **13**, 1526-1530.

117 S. Bai, S. Q. Chen, X. P. Shen, G. X. Zhu and G. X. Wang, *RSC Adv.*, 2012, **2**, 10977-10984.

118 R. H. Wang, C. H. Xu, J. Sun, L. Gao and C. C. Lin, *J. Mater. Chem. A*, 2013, **1**, 1794-1800.

119 H. L. Wang, L. F. Cui, Y. Yang, H. S. Casalongue, J. T. Robinson, Y. Y. Liang, Y. Cui and H. J. Dai, *J. Am. Chem. Soc.*, 2010, **132**, 13978-13980.

120 D. F. Qiu, L. Y. Ma, M. B. Zheng, Z. X. Lin, B. Zhao, Z. Wen, Z. B. Hu, L. Pu and Y. Shi, *Mater. Lett.*, 2012, **84**, 9-12.

121 Y. J. Mai, D. Zhang, Y. Q. Qiao, C. D. Gu, X. L. Wang and J. P. Tu, *J. Power Sources*, 2012, **216**, 201-207.

122 S. Y. Liu, J. Xie, Y. X. Zheng, G. S. Cao, T. J. Zhu and X. B. Zhao, *Electrochim. Acta*, 2012, **66**, 271-278.

123 S. Mao, Z. H. Wen, H. Kim, G. H. Lu, P. Hurley and J. H. Chen, *ACS Nano*, 2012, **6**, 7505-7513.

124 I. Nam, N. D. Kim, G. P Kim, J. Park and J. Yi, *J. Power Sources*, 2013, **244**, 56-62.

125 L. Li, Z. P. Guo, A. J. Du and H. K. Liu, *J. Mater. Chem.*, 2012, **22**, 3600-3605.

126 C. Chen, H. Jian, X. X. Fu, Z. M. Ren, M. Yan, G. D. Qian and Z. Y. Wang, *RSC Adv.*, 2014, **4**, 5367-5370.

127 X. L. Li, H. F. Song, H. Wang, Y. L. Zhang, K. Du, H. Y. Li and J. M. Huang, *J. Appl. Electrochem.*, 2012, **42**, 1065-1070.

128 N. Lavoie, P. R. L. Malenfant, F. M. Courtel, Y. Abu-Lebdeh and I. J. Davidson, *J. Power Sources*, 2012, **213**, 249-254.

129 T. H. Wu, F. Y. Tu, S. Q. Liu, S. X. Zhuang, G. H. Jin and C. Y. Pan, *J. Mater. Sci.*, 2014, **49**, 1861-1867.

130 A. P. Yu, H. W. Park, A. Davies, D. C. Higgins, Z. W. Chen and X. C. Xiao, *J. Phys. Chem. Lett.*, 2011, **2**, 1855-1860.

131 Y. M. Sun, X. L. Hu, W. Luo, F. F. Xia and Y. H. Huang, *Adv. Funct. Mater.*, 2013, **23**, 2436-2444.

132 T. Hu, X. Sun, H. T. Sun, M. P. Yu, F. Y. Lu, C. S. Liu and J. Lian, *Carbon*, 2013, **51**, 322-326.

133 M. M. Zhen, L. W. Su, Z. H. Yuan, L. Liu and Z. Zhou, *RSC Adv.*, 2013, **3**, 13696-13701.

134 H. C. Tao, L. Z. Fan, X. Q. Yan and X. H. Qu, *Electrochim. Acta*, 2012, **69**, 328-333.

135 D. D. Cai, P. C. Lian, X. F. Zhu, S. Z. Liang, W. S. Yang and H. H. Wang, *Electrochim. Acta*, 2012, **74**, 65-72.

136 W. Li, F. Wang, S. S. Feng, J. X. Wang, Z. K. Sun, B. Li, Y. H. Li, J. P. Yang, A. A. Elzatahry, Y. Y. Xia and D. Y. Zhao, *J. Am. Chem. Soc.*, 2013, **135**, 18300-18303.

137 D. H. Wang, D. Choi, J. Li, Z. G. Yang, Z. M. Nie, R. Kou, D. H. Hu, C. M. Wang, L. V. Saraf, J. G. Zhang, I. A. Aksay and J. Liu, *ACS Nano*, 2009, **3**, 907-914.

138 H. Q. Cao, B. J. Li, J. X. Zhang, F. Lian, X. H. Kong and M. Z. Qu, *J. Mater. Chem.*, 2012, **22**, 9759-9766.

139 N. Li, G. M. Zhou, R. P. Fang, F. Li and H. M. Cheng, *Nanoscale*, 2013, **5**, 7780-7784.

140 Z. Zhang, Q. X. Chu, H. Y. Li, J. H. Hao, W. S. Yang, B. P. Lu, X. Ke, J. Li and J. L. Tang, *J. Colloid Interface Sci.*, 2013, **409**, 38-42.

141 Y. F. Tang, F. Q. Huang, W. Zhao, Z. Q. Liu and D. Y. Wan, *J. Mater. Chem.*, 2012, **22**, 11257-11260.

142 S. J. Ding, J. S. Chen, D. Y. Luan, F. Y. C. Boey, S. Madhavi and X. W. Lou, *Chem. Commun.*, 2011, **47**, 5780-5782.

143 H. Huang, J. W. Fang, Y. Xia, X. Y. Tao, Y. P. Gan, J. Du, W. J. Zhu and W. K. Zhang, *J. Mater. Chem. A*, 2013, **1**, 2495-2500.

144 L. F. He, R. G. Ma, N. Du, J. G. Ren, T. L. Wong, Y. Y. Li and S. T. Lee, *J. Mater. Chem.*, 2012, **22**, 19061-19066.

145 J. Wang, Y. K. Zhou, B. Xiong, Y. Y. Zhao, X. J. Huang and Z. P. Shao, *Electrochim. Acta*, 2013, **88**, 847-857.

146 X. Xin, X. F. Zhou, J. H. Wu, X. Y. Yao and Z. P. Liu, *ACS Nano*, 2012, **6**, 11035-11043.

147 W. H. Shi, X. H. Rui, J. X. Zhu and Q. Y. Yan, *J. Phys. Chem. C*, 2012, **116**, 26685-26693.

148 Y. Sun, S. B. Yang, L. P. Lv, I. Lieberwirth, L. C. Zhang, C. X. Ding and C. H. Chen, *J. Power Sources*, 2013, **241**, 168-172.

149 Y. Q. Qian, A. Vu, W. Smyrl and A. Stein, *J. Electrochem. Soc.*, 2012, **159**, A1135-A1140.

150 H. Gwon, H. S. Kim, K. U. Lee, D. H. Seo, Y. C. Park, Y. S. Lee, B. T. Ahn and K. Kang, *Energy Environ. Sci.*, 2011, **4**, 1277-1283.

151 H. M. Liu and W. S. Yang, *Energy Environ. Sci.*, 2011, **4,** 4000-4008.

152 Z. L. Wang, D. Xu, Y. Huang, Z. Wu, L. M. Wang and X. B. Zhang, *Chem. Commun.*, 2012, **48**, 976-978.

153 J. W. Lee, S. Y. Lim, H. M. Jeong, T. H. Hwang, J. K. Kang and J. W. Choi, *Energy Environ. Sci.*, 2012, **5**, 9889-9894.

154 J. L. Cheng, B. Wang, H. L. L. Xin, G. C. Yang, H. Q. Cai, F. D. Nie and H. Huang, *J. Mater. Chem. A*, 2013, **1**, 10814-10820.

155 X. H. Rui, J. X. Zhu, D. H. Sim, C. Xu, Y. Zeng, H. H. Hng, T. M. Lim and Q. Y. Yan, *Nanoscale*, 2011, **3**, 4752-4758.

156 G. D. Du, K. H. Seng, Z. P. Guo, J. Liu, W. X. Li, D. Z. Jia, C. Cook, Z. W. Liu and H. K. Liu, *RSC Adv.*, 2011, **1**, 690-697.

157 F. X. Wang, S. Y. Xiao, Y. Y. Hou, C. L. Hu, L. L. Liu and Y. P. Wu, *RSC Adv.*, 2013, **3**, 13059-13084.

158 S. B. Yang, Y. J. Gong, Z. Liu, L. Zhan, D. P. Hashim, L. L. Ma, R. Vajtai and P. M. Ajayan, *Nano Lett.*, 2013, **13**, 1596-1601.

159 C. Nethravathi, B. Viswanath, J. Michael and M. Rajamath, *Carbon*, 2012, **50**, 4839-4846.

160 C. Nethravathi, C. R. Rajamathi, M. Rajamathi, U. K. Gautam, X. Wang, D. Golberg and Y. Bando, *ACS Appl. Mater. Interfaces*, 2013, **5**, 2708-2714.

161 H. B. Zhao, L. Y. Pan, S. Y. Xing, J. Luo and J. Q. Xu, *J. Power Sources*, 2013, **222**, 21-31.

162 Y. Shi, S. L. Chou, J. Z. Wang, H. J. Li, H. K. Liu and Y. P. Wu, *J. Power Sources*, 2013, **244**, 684-689.

163 L. Q. Mai, Q. L. Wei, Q. Y. An, X. C. Tian, Y. L. Zhao, X. Xu, L. Xu, L. Chang and Q. J. Zhang, *Adv. Mater.*, 2013, **25**, 2969-2973.

164 Y. M. Sun, X. L. Hu, W. Luo and Y. H. Huang, *ACS Nano*, 2011, **5**, 7100-7107.

165 S. H. Choi and Y. C. Kang, *ChemSusChem*, 2014, **7**, 523-528.

166 A. Bhaskar, M. Deepa, T. N. Rao and U. V. Varadaraju, *J. Power Sources*, 2012, **216**, 169-178.

167 K. H. Seng, G. D. Du, L. Li, Z. X. Chen, H. K. Liu and Z. P. Guo, *J. Mater. Chem.*, 2012, **22**, 16072-16077.

168 P. X. Han, W. Ma, S. P. Pang, Q. S. Kong, J. H. Yao, C. F. Bi and G. L. Cui, *J. Mater. Chem. A*, 2013, **1**, 5949-5954.

169 Y. J. Chen, X. P. Di, C. Ma, C. L. Zhu, P. Gao, J. Q. Li, C. W. Sun and Q. Y. Ouyang, *RSC Adv.*, 2013, **3**, 17659-17663.

170 F. F. Xia, X. L. Hu, Y. M. Sun, W. Luo and Y. H. Huang, *Nanoscale*, 2012, **4**, 4707-4711.

171 Q. W. Tang, Z. Q. Shan, L. Wang and X. Qin, *Electrochim. Acta*, 2012, **79**, 148-153.

172 C. L. Liu, Y. Wang, C. Zhang, X. S. Li and W. S. Dong, *Mater. Chem. Phys.*, 2014, **143**, 1111-1118.

173 L. Noerochim, J. Z. Wang, D. Wexler, Z. Chao and H. K. Liu, *J. Power Sources*, 2013, **228**, 198-205.

174 Q. W. Tang, L. Wang, K. L. Zhu, Z. Q. Shan and X. Qin, *Mater. Lett.*, 2013, **100**, 127-129.

175 Y. F. Dong, S. Li, H. M. Xu, M. Y. Yan, X. M. Xu, X. C. Tian, Q. Liu and L. Q. Mai, *Phys. Chem. Chem. Phys.*, 2013, **15**, 17165-17170.

176 C. T. Hsieh, C. Y. Lin, Y. F. Chen and J. S. Lin, *Electrochim. Acta*, 2013, **111**, 359-365.

177 M. P. Yu, D. L. Shao, F. Y. Lu, X. Sun, H. T. Sun, T. Hu, G. K. Wang, S. Sawyer, H. Qiu and J. Lian, *Electrochem. Commun.*, 2013, **34**, 312-315.

178 W. T. Song, J. Xie, S. Y. Liu, Y. X. Zheng, G. S. Cao, T. J. Zhu and X. B. Zhao, *Int. J. Electrochem. Sci.*, 2012, **7**, 2164-2174.

179 C. D. Wang, Y. Li, Y. S. Chui, Q. H. Wu, X. F. Chen and W. J. Zhang, *Nanoscale*, 2013, **5**, 10599-10604.

180 S. Q. Chen, Y. Wang, H. Ahn and G. X. Wang, *J. Power Sources*, 2012, **216**, 22-27.

181 W. B. Yue, S. Yang, Y. L. Liu and X. J. Yang, *Mater. Res. Bull.*, 2013, **48**, 1575-1580.

182 X. Y. Zhou, Y. L. Zou and J. Yang, *J. Power Sources*, 2014, **253**, 287-293.

183 N. Li, H. W. Song, H. Cui and C. X. Wang, *Nano Energy*, 2014, **3**, 102-112.
184 G. X. Wang, B. Wang, X. L. Wang, J. Park, S. X. Dou, H. Ahn and K. Kim, *J. Mater. Chem.*, 2009, **19**, 8378-8384.
185 E. G. Bae, Y. H. Hwang and M. Pyo, *Bull. Korean Chem. Soc.*, 2013, **34**, 1199-1204.
186 Y. Q. Zou and Y. Wang, *ACS Nano*, 2011, **5**, 8108-8114.
187 B. Luo, B. Wang, M. H. Liang, J. Ning, X. L. Li and L. J. Zhi, *Adv. Mater.*, 2012, **24**, 1405-1409.
188 C. Wang, J. Ju, Y. Q. Yang, Y. F. Tang, H. Bi, F. H. Liao, J. H. Lin, Z. J. Shi, F. Q. Huang and R. P. S. Han, *RSC Adv.*, 2013, **3**, 21588-21595.
189 L. W. Ji, Z. K. Tan, T. Kuykendall, E. J. An, Y. B. Fu, V. Battaglia and Y. G. Zhang, *Energy Environ. Sci.*, 2011, **4**, 3611-3616.
190 B. Luo, B. Wang, X. L. Li, Y. Y. Jia, M. H. Liang and L. J. Zhi, *Adv. Mater.*, 2012, **24**, 3538-3543.
191 H. L. Lu, N. W. Li, M. B. Zheng, L. Qiu, S. T. Zhang, J. F. Zheng, G. B. Ji and J. M. Cao, *Mater. Lett.*, 2014, **115**, 125-128.
192 X. F. Li, X. B. Meng, J. Liu, D. S. Geng, Y. Zhang, M. N. Banis, Y. L. Li, J. L. Yang, R. Y. Li, X. L. Sun, M. Cai and M. W. Verbrugge, *Adv. Funct. Mater.*, 2012, **22**, 1647-1654.
193 S. J. R. Prabakar, Y. H. Hwang, E. G. Bae, S. Shim, D. Kim, M. S. Lah, K. S. Sohn and M. Pyo, *Adv. Mater.*, 2013, **25**, 3307-3312.
194 Q. Guo, Z. Zheng, H. L. Gao, J. Ma and X. Qin, *J. Power Sources*, 2013, **240**, 149-154.
195 Q. Guo and X. Qin, *ECS Solid State Lett.*, 2013, **2**, M41-M43.
196 J. Lin, Z. W. Peng, C. S. Xiang, G. D. Ruan, Z. Yan, D. Natelson and J. M. Tour, *ACS Nano*, 2013, **7**, 6001-6006.
197 J. Liu, J. M. Huang, L. L. Hao, H. D. Liu and X. L. Li, *Ceram. Int.*, 2013, **39**, 8623-8627.
198 J. S. Zhu, D. L. Wang, L. Wang, X. S. Lang and W. L. You, *Electrochim. Acta*, 2013, **91**, 323-329.
199 B. P. Vinayan and S. Ramaprabhu, *J. Mater. Chem. A*, 2013, **1**, 3865-3871.
200 X. S. Zhou, L. J. Wan and Y. G. Guo, *Adv. Mater.*, 2013, **25**, 2152-2157.
201 J. F. Liang, Y. K. Liu, L. Guo and L. D. Li, *RSC Adv.*, 2013, **3**, 11489-11492.
202 B. J. Li, H. Q. Cao, J. X. Zhang, M. Z. Qu, F. Lian and X. H. Kong, *J. Mater. Chem.*, 2012, **22**, 2851-2854.
203 T. Q. Chen, L. K. Pan, X. J. Liu, K. Yu and Z. Sun, *RSC Adv.*, 2012, **2**, 11719-11724.
204 H. J. Song, L. C. Zhang, C. L. He, Y. Qu, Y. F. Tian and Y. Lv, *J. Mater. Chem.*, 2011, **21**, 5972-5977.
205 J. X. Zhu, Z. Y. Lu, M. O. Oo, H. H. Hng, J. Ma, H. Zhang and Q. Y. Yan, *J. Mater. Chem.*, 2011, **21**, 12770-12776.
206 G. Ji, B. Ding, Z. Sha, J. S. Wu, Y. Ma and J. Y. Lee, *Nanoscale*, 2013, **5**, 5965-5972.
207 Y. X. Wang, Y. G. Lim, M. S. Park, S. L. Chou, J. H. Kim, H. K. Liu, S. X. Dou and Y. J. Kim, *J. Mater. Chem. A*, 2014, **2**, 529-534.
208 A. K. Yang, Y. Xue, Y. Zhang, X. F. Zhang, H. Zhao, X. J. Li, Y. J. He and Z. B. Yuan, *J. Mater. Chem. B*, 2013, **1**, 1804-1811.
209 S. K. Park, S. H. Yu, N. Pinna, S. Woo, B. Jang, Y. H. Chung, Y. H. Cho, Y. E. Sung and Y. Z. Piao, *J. Mater. Chem.*, 2012, **22**, 2520-2525.
210 S. M. Paek, E. Yoo and I. Honma, *Nano Lett.*, 2009, **9**, 72-75.
211 Y. Q. Zhu, C. Li and C. B. Cao, *RSC Adv.*, 2013, **3**, 11860-11868.
212 Y. H. Hwang, E. G. Bae, K. S. Sohn, S. Shim, X. K. Song, M. S. Lah and M. Pyo, *J. Power Sources*, 2013, **240**, 683-690.
213 X. S. Zhou, Y. X. Yin, L. J. Wan and Y. G. Guo, *J. Mater. Chem.*, 2012, **22**, 17456-17459.
214 Y. C. Yang, X. B. Ji, F. Lu, Q. Y. Chen and C. E. Banks, *Phys. Chem. Chem. Phys.*, 2013, **15**, 15098-15105.
215 R. L. Liang, H. Q. Cao, D. Qian, J. X. Zhang and M. Z. Qu, *J. Mater. Chem.*, 2011, **21**, 17654-17657.
216 B. Zhang, Q. B. Zheng, Z. D. Huang, S. W. Oh and J. K. Kim, *Carbon*, 2011, **49**, 4524-4534.
217 J. L. Cheng, H. L. Xin, H. M. Zheng and B. Wang, *J. Power Sources*, 2013, **232**, 152-158.
218 C. F. Zhang, X. Peng, Z. P. Guo, C. B. Cai, Z. X. Chen, D. Wexler, S. Li and H. K. Liu, *Carbon*, 2012, **50**, 1897-1903.
219 J. F. Liang, W. Wei, D. Zhong, Q. L. Yang, L. D. Li and L. Guo, *ACS Appl. Mater. Interfaces*, 2012, **4**, 454-459.
220 S. J. Ding, D. Y. Luan, F. Y. C. Boey, J. S. Chen and X. W. Lou, *Chem. Commun.*, 2011, **47**, 7155-7157.
221 H. D. Liu, J. M. Huang, C. J. Xiang, J. Liu and X. L. Li, *J. Mater. Sci.: Mater. Electron.*, 2013, **24**, 3640-3645.
222 C. H. Xu, J. Sun and L. Gao, *J. Mater. Chem.*, 2012, **22**, 975-979.
223 Q. Y. Han, J. T. Zai, Y. L. Xiao, B. Li, M. Xu and X. F. Qian, *RSC Adv.*, 2013, **3**, 20573-20578.
224 C. H. Xu, J. Sun and L. Gao, *Nanoscale*, 2012, **4**, 5425-5430.
225 H. D. Liu, J. M. Huang, X. L. Li, J. Liu, Y. X. Zhang and K. Du, *Appl. Surf. Sci.*, 2012, **258**, 4917-4921.
226 N. Mahmood, C. Z. Zhang, F. Liu, J. H. Zhu and Y. L. Hou, *ACS Nano*, 2013, **7**, 10307-10318.
227 B. Feng, J. Xie, G. S. Cao, T. J. Zhu and X. B. Zhao, *New J. Chem.*, 2013, **37**, 474-480.
228 J. Z. Chen, L. Yang, S. H. Fang, Z. X. Zhang and S. I. Hirano, *Electrochim. Acta*, 2013, **105**, 629-634.
229 P. Chen, L. Guo and Y. Wang, *J. Power Sources*, 2013, **222**, 526-532.
230 S. Q. Chen, P. Chen, M. H. Wu, D. Y. Pan and Y. Wang, *Electrochem. Commun.*, 2010, **12**, 1302-1306.
231 H. X. Yang and L. Li, *J. Alloys Compd.*, 2014, **584**, 76-80.
232 X. L. Li and L. J. Zhi, *Nanoscale*, 2013, **5**, 8864-8873.
233 X. Zhao, C. M. Hayner, M. C. Kung and H. H. Kung, *Adv. Energy Mater.*, 2011, **1**, 1079-1084.
234 X. Xin, X. F. Zhou, F. Wang, X. Y. Yao, X. X. Xu, Y. M. Zhu and Z. P. Liu, *J. Mater. Chem.*, 2012, **22**, 7724-7730.
235 F. Sun, K. Huang, X. Qi, T. Gao, Y. P. Liu, X. H. Zou, X. L. Wei and J. X. Zhong, *Nanoscale*, 2013, **5**, 8586-8592.
236 C. F. Guo, D. L. Wang, T. F. Liu, J. S. Zhu and X. S. Lang, *J. Mater. Chem. A*, 2014, **2**, 3521-3527.
237 S. N. Yang, G. R. Li, Q. Zhu and Q. M. Pan, *J. Mater. Chem.*, 2012, **22**, 3420-3425.
238 G. Y. Zhao, L. Zhang, Y. F. Meng, N. Q. Zhang and K. N. Sun, *J. Power Sources*, 2013, **240**, 212-218.
239 M. R. Su, Z. X. Wang, H. J. Guo, X. H. Li, S. L. Huang, W. Xiao and L. Gan, *Electrochim. Acta*, 2014, **116**, 230-236.
240 M. Zhou, F. Pu, Z. Wang, T. W. Cai, H. Chen, H. Y. Zhang and S. Y. Guan, *Phys. Chem. Chem. Phys.*, 2013, **15**, 11394-11401.
241 X. S. Zhou, Y. X. Yin, L. J. Wan and Y. G. Guo, *Chem. Commun.*, 2012, **48**, 2198-2200.
242 M. Zhou, T. W. Cai, F. Pu, H. Chen, Z. Wang, H. Y. Zhang and S. Y. Guan, *ACS Appl. Mater. Interfaces*, 2013, **5**, 3449-3455.
243 J. Y. Ji, H. X. Ji, L. L. Zhang, X. Zhao, X. Bai, X. B. Fan, F. B. Zhang and R. S. Ruoff, *Adv. Mater.*, 2013, **25**, 4673-4677.
244 C. D. Wang, Y. S. Chui, R. G. Ma, T. L. Wong, J. G. Ren, Q. H. Wu, X. F. Chen and W. J. Zhang, *J. Mater. Chem. A*, 2013, **1**, 10092-10098.
245 S. Q. Chen, P. T. Bao, X. D. Huang, B. Sun and G. X. Wang, *Nano Res.*, 2014, **7**, 85-94.
246 J. K. Lee, K. B. Smith, C. M. Hayner and H. H. Kung, *Chem. Commun.*, 2010, **46**, 2025-2027.
247 Y. S. Ye, X. L. Xie, J. Rick, F. C. Chang and B. J. Hwang, *J. Power Sources*, 2014, **247**, 991-998.
248 J. B. Chang, X. K. Huang, G. H. Zhou, S. M. Cui, P. B. Hallac, J. W. Jiang, P. T. Hurley and J. H. Chen, *Adv. Mater.*, 2014, **26**, 758-764.
249 Y. S. He, P. F. Gao, J. Chen, X. W. Yang, X. Z. Liao, J. Yang and Z. F. Ma, *RSC Adv.*, 2011, **1**, 958-960.
250 L. Zhang, W. W. Hao, H. B. Wang, L. F. Zhang, X. M. Feng, Y. B. Zhang, W. X. Chen, H. Pang and H. H. Zheng, *J. Mater. Chem. A*, 2013, **1**, 7601-7611.
251 R. C. de Guzman, J. H. Yang, M. M. C. Cheng, S. O. Salley and K. Y. S. Ng, *J. Mater. Sci.*, 2013, **48**, 4823-4833.
252 X. S. Zhou, Y. X. Yin, L. J. Wan and Y. G. Guo, *Adv. Energy Mater.*, 2012, **2**, 1086-1090.
253 H. C. Tao, L. Z. Fan, Y. F. Mei and X. H. Qu, *Electrochem. Commun.*, 2011, **13**, 1332-1335.
254 X. S. Zhou, A. M. Cao, L. J. Wan and Y. G. Guo, *Nano Res.*, 2012, **5**, 845-853.

255 J. Z. Wang, C. Zhong, S. L. Chou and H. K. Liu, *Electrochem. Commun.*, 2010, **12**, 1467-1470.
256 H. Li, C. X. Lu, C. L. Ma and B. P. Zhang, *Funct. Mater. Lett.*, 2014, **7**, 1350067.
257 S. M. Zhu, C. L. Zhu, J. Ma, Q. Meng, Z. P. Guo, Z. Y. Yu, T. Lu, Y. Li, D. Zhang and W. M. Lau, *RSC Adv.*, 2013, **3**, 6141-6146.
258 H. Li and C. X. Lu, *Funct. Mater. Lett.*, 2013, **6**, 1350063.
259 Y. J. Du, G. N. Zhu, K. Wang, Y. G. Wang, C. X. Wang and Y. Y. Xia, *Electrochem. Commun.*, 2013, **36**, 107-110.
260 D. P. Wong, H. P. Tseng, Y. T. Chen, B. J. Hwang, L. C. Chen and K. H. Chen, *Carbon*, 2013, **63**, 397-403.
261 Y. Yang, J. G. Ren, X. Wang, Y. S. Chui, Q. H. Wu, X. F. Chen and W. J. Zhang, *Nanoscale*, 2013, **5**, 8689-8694.
262 Z. Y. Lu, J. X. Zhu, D. H. Sim, W. H. Shi, Y. Y. Tay, J. Ma, H. H. Hng and Q. Y. Yan, *Electrochim. Acta*, 2012, **74**, 176-181.
263 Y. H. Zhu, W. Liu, X. Y. Zhang, J. C. He, J. T. Chen, Y. P. Wang and T. B. Cao, *Langmuir*, 2013, **29**, 744-749.
264 J. G. Ren, C. D. Wang, Q. H. Wu, X. Liu, Y. Yang, L. F. He and W. J. Zhang, *Nanoscale*, 2014, **6**, 3353-3360.
265 L. W. Ji, H. H. Zheng, A. Ismach, Z. K. Tan, S. D. Xun, E. Lin, V. Battaglia, V. Srinivasan and Y. G. Zhang, *Nano Energy*, 2012, **1**, 164-171.
266 D. Li, K. H. Seng, D. Q. Shi, Z. X. Chen, H. K. Liu and Z. Q. Guo, *J. Mater. Chem. A*, 2013, **1**, 14115-14121.
267 C. Zhong, J. Z. Wang, X. W. Gao, D. Wexler and H. K. Liu, *J. Mater. Chem. A*, 2013, **1**, 10798-10804.
268 J. S. Cheng and J. Du, *CrystEngComm*, 2012, **14**, 397-400.
269 J. G. Ren, Q. H. Wu, H. Tang, G. Hong, W. J. Zhang and S. T. Lee, *J. Mater. Chem. A*, 2013, **1**, 1821-1826.
270 D. J. Xue, S. Xin, Y. Yan, K. C. Jiang, Y. X. Yin, Y. G. Guo and L. J. Wan, *J. Am. Chem. Soc.*, 2012, **134**, 2512-2515.
271 W. Wei and L. Guo, *Part. Part. Syst. Charact.*, 2013, **30**, 658-661.
272 D. Q. Lv, M. L. Gordin, R.Yi, T. Xu, J. X. Song, Y. B. Jiang, D. Choi and D. H. Wang, *Adv. Funct. Mater.*, 2014, **24**, 1059-1066.
273 C. D. Wang, Y. S. Chui, Y. Li, X. F. Chen and W. J. Zhang, *Appl. Phys. Lett.*, 2013,**103**, 253903.
274 C. Wang, J. Ju, Y. Q. Yang, Y. F. Tang, J. H. Lin, Z. J. Shi, R. P. S. Han and F. Q. Huang, *J. Mater. Chem. A*, 2013, **1**, 8897-8902.
275 H. Kim, Y. Son, C. Park, J. Cho and H. C. Choi, *Angew. Chem. Int. Ed.*, 2013, **52**, 5997 -6001.
276 K. Chang and W. X. Chen, *ACS Nano*, 2011, **5**, 4720-4728.
277 K. Chang and W. X. Chen, *Chem. Commun.*, 2011, **47**, 4252-4254.
278 X. S. Zhou, L. J. Wan and Y. G. Guo, *Chem. Commun.*, 2013, **49**, 1838-1840.
279 H. L. Yu, C. Ma, B. H. Ge, Y. J. Chen, Z. Xu, C. L. Zhu, C. Y. Li, Q. Y. Ouyang, P. Gao, J. Q. Li, C. W. Sun, L. H. Qi, Y. M. Wang and F. H. Li, *Chem. Eur. J.*, 2013, **19**, 5818-5823.
280 K. Zhang, H. J. Kim, X. J. Shi, J. T. Lee, J. M. Choi, M. S. Song and J. H. Park, *Inorg. Chem.*, 2013, **52**, 9807-9812.
281 Y. H. Hu, X. F. Li, A. Lushington, M. Cai, D. S. Geng, M. N. Banis, R. Y. Li and X. L. Sun, *ECS J. Solid State Sci. Technol.*, 2013, **2**, M3034-M3039.
282 J. Xiao, X. J. Wang, X. Q. Yang, S. D. Xun, G. Liu, P. K. Koech, J. Liu and J. P. Lemmon, *Adv. Funct. Mater.*, 2011, **21**, 2840-2846.
283 Z. Wang, L. Ma, W. X. Chen, G. C. Huang, D. Y. Chen, L. B. Wang and J. Y. Lee, *RSC Adv.*, 2013, **3**, 21675-21684.
284 V. H. Pham, K. H. Kim, D. W. Jung, K. Singh, E. S. Oh and J. S. Chung, *J. Power Sources*, 2013, **244**, 280-286.
285 X. F. Zhou, Z. Wang, W. X. Chen, L. Ma, D. Y. Chen and J. Y. Lee, *J. Power Sources*, 2014, **251**, 264-268.
286 Y. T. Liu, X. D. Zhu, Z. Q. Duan and X. M. Xie, *Chem. Commun.*, 2013, **49**, 10305-10307.
287 L. Ma, G. C. Huang, W. X. Chen, Z. Wang, J. B. Ye, H. Y. Li, D. Y. Chen and J. Y. Lee, *J. Power Sources*, 2014, **264**, 262-271.
288 G. C. Huang, T. Chen, W. X. Chen, Z. Wang, K. Chang, L. Ma, F. H. Huang, D. Y. Chen and J. Y. Lee, *Small*, 2013, **9**, 3693-3703.
289 K. Chang and W. X. Chen, *J. Mater. Chem.*, 2011, **21**, 17175-17184.
290 Z. Wang, T. Chen, W. X. Chen, K. Chang, L. Ma, G. C. Huang, D. Y. Chen and J. Y. Lee, *J. Mater. Chem. A*, 2013, **1**, 2202-2210.
291 L. W. Ji, H. L. L. Xin, T. R. Kuykendall, S. L. Wu, H. M. Zheng, M. M. Rao, E. J. Cairns, V. Battaglia and Y. G. Zhang, *Phys. Chem. Chem. Phys.*, 2012, **14**, 6981-6986.
292 N. Du, X. L. Wu, C. X. Zhai, H. Zhang and D. R. Yang, *J. Alloys Compd.*, 2013, **580**, 457-464.
293 M. Zhang, D. N. Lei, X. Z. Yu, L. B. Chen, Q. H. Li, Y. G. Wang, T. H. Wang and G. Z. Cao, *J. Mater. Chem.*, 2012, **22**, 23091-23097.
294 L. Mei, C. Xu, T. Yang, J. M. Ma, L. B. Chen, Q. H. Li and T. H. Wang, *J. Mater. Chem. A*, 2013, **1**, 8658-8664.
295 J. F. Yin, H. Q. Cao, Z. F. Zhou, J. X. Zhang and M. Z. Qu, *J. Mater. Chem.*, 2012, **22**, 23963-23970.
296 M. Sathish, S. Mitani, T. Tomai and I. Honma, *J. Phys. Chem. C*, 2012, **116**, 12475-12481.
297 C. F. Shen, L. Y. Ma, M. B. Zheng, B. Zhao, D. F. Qiu, L. J. Pan, J. M. Cao and Y. Shi, *J. Solid State Electrochem.*, 2012, **16**, 1999-2004.
298 X. Jiang, X. L. Yang, Y. H. Zhu, J. H. Shen, K. C. Fan and C. Z. Li, *J. Power Sources*, 2013, **237**, 178-186.
299 P. Chen, Y. Su, H. Liu and Y. Wang, *ACS Appl. Mater. Interfaces*, 2013, **5**, 12073-12082.
300 S. Y. Liu, X. Lu, J. Xie, G. S. Cao, T. J. Zhu and X. B. Zhao, *ACS Appl. Mater. Interfaces*, 2013, **5**, 1588-1595.
301 B. Luo, Y. Fang, B. Wang, J. S. Zhou, H. H. Song and L. J. Zhi, *Energy Environ. Sci.*, 2012, **5**, 5226-5230.
302 Z. F. Jiang, C. Wang, G. H. Du, Y. J. Zhong and J. Z. Jiang, *J. Mater. Chem.*, 2012, **22**, 9494-9496.
303 K. Chang, Z. Wang, G. C. Huang, H. Li, W. X. Chen and J. Y. Lee, *J. Power Sources*, 2012, **201,** 259-266.
304 L. H. Zhuo, Y. Q. Wu, L. Y. Wang, Y. C. Yu, X. B. Zhang and F. Y. Zhao, *RSC Adv.*, 2012, **2**, 5084-5087.
305 N. Mahmood, C. Z. Zhang, J. Jiang, F. Liu and Y. L. Hou, *Chem. Eur. J.*, 2013, **19**, 5183-5190.
306 Q. Pan, J. Xie, S. Y. Liu, G. S. Cao, T. J. Zhu and X. B. Zhao, *RSC Adv.*, 2013, **3**, 3899-3906.
307 Y. Gu, Y. Xu and Y. Wang, *ACS Appl. Mater. Interfaces*, 2013, **5**, 801-806.
308 J. Xie, S. Y. Liu, G. S. Cao, T. J. Zhu and X. B. Zhao, *Nano Energy*, 2013, **2**, 49-56.
309 G. C. Huang, T. Chen, Z. Wang, K. Chang and W. X. Chen, *J. Power Sources*, 2013, **235**, 122-128.
310 F. M. Ye, G. H. Du, Z. F. Jiang, Y. J. Zhong, X. D. Wang, Q. P. Cao and J. Z. Jiang, *Nanoscale*, 2012, **4**, 7354-7357.
311 X. Yang, C. Y. Chan, H. T. Xue, J. Xu, Y. B. Tang, Q. Wang, T. L. Wong and C. S. Lee, *CrystEngComm*, 2013, **15**, 6578-6584.
312 P. V. Prikhodchenko, J. Gun, S. Sladkevich, A. A. Mikhaylov, O. Lev, Y. Y. Tay, S. K. Batabyal and D. Y. W. Yu, *Chem. Mater.*, 2012, **24**, 4750-4757.
313 G. D. Nie, L. Zhang, X. F. Lu, X. J. Bian, W. N. Sun and C. Wang, *Dalton Trans.*, 2013, **42**, 14006-14013.
314 L. Fei, Q. L. Lin, B. Yuan, G. Chen, P. Xie, Y. L. Li, Y. Xu, S. G. Deng, S. Smirnov and H. M. Luo, *ACS Appl. Mater. Interfaces*, 2013, **5**, 5330-5335.
315 X. D. Xu, C. S. Rout, J. Yang, R. G. Cao, P. Oh, H. S. Shin and J. Cho, *J. Mater. Chem. A*, 2013, **1**, 14548-14554.
316 D. Y. Chen, G. Ji, B. Ding, Y. Ma, B. H. Qu, W. X. Chen and J. Y. Lee, *Nanoscale*, 2013, **5**, 7890-7896.
317 D. Z. Chen, H. Y. Quan, G. S. Wang and L. Guo, *ChemPlusChem*, 2013, **78**, 843-851.
318 S. Q. Chen, P. Chen and Y. Wang, *Nanoscale*, 2011, **3**, 4323-4329.
319 S. H. Bae, K. Karthikeyan, Y. S. Lee and I. K. Oh, *Carbon*, 2013, **64**, 527-536.
320 M. Q. Zhao, X. F. Liu, Q. Zhang, G. L. Tian, J. Q. Huang, W. C. Zhu and F. Wei, *ACS Nano*, 2012, **6**, 10759-10769.
321 Y. H. Hu, X. F. Li, J. J. Wang, R. Y. Li and X. L. Sun, *J. Power Sources*, 2013, **237**, 41-46.
322 W. Wang, I. Ruiz, S. R. Guo, Z. Favors, H. H. Bay, M. Ozkan and C. S. Ozkan, *Nano Energy*, 2014, **3**, 113-118.
323 S. Q. Chen, P. T. Bao and G. X. Wang, *Nano Energy*, 2013, **2**, 425-434.
324 L. F. Shen, X. G. Zhang, H. S. Li, C. Z. Yuan and G. Z. Cao, *J. Phys. Chem. Lett.*, 2011, **2**, 3096-3101.

325 S. H. Lee, V. Sridhar, J. H. Jung, K. Karthikeyan, Y. S. Lee, R. Mukherjee, N. Koratkar and I. K. Oh, *ACS Nano*, 2013, **7**, 4242-4251.
326 J. L. Liu, J. B. Jiang, D. Qian, G. R. Tan, S. J. Peng, H. M. Yuan, D. M. Luo, Q. F. Wang and Y. C. Liu, *RSC Adv.*, 2013, **3,** 15457-15466.
327 G. Wu, Y. K. Zhou and Z. P. Shao, *Appl. Surf. Sci.*, 2013, **283**, 999-1005.
328 J. Zhang, F. Zhao, Z. P. Zhang, N. Chen and L. T. Qu, *Nanoscale*, 2013, **5**, 3112-3126.
329 Z. S. Wu, W. C. Ren, L. Xu, F. Li and H. M. Cheng, *ACS Nano*, 2011, **5**, 5463-5471.
330 X. L. Wang, Z. Zeng, H. Ahn and G. X. Wang, *Appl. Phys. Lett.*, 2009, **95**, 183103.
331 J. Ha, S. K. Park, S. H. Yu, A. H. Jin, B. Jang, S. Bong, I. Kim, Y. E. Sung and Y. Z. Piao, *Nanoscale*, 2013, **5**, 8647-8655.
332 M. A. Worsley, P. J. Pauzauskie, T. Y. Olson, J. Biener, J. H. Satcher, Jr. and T. F. Baumann, *J. Am. Chem. Soc.*, 2010, **132**, 14067-14069.
333 Y. R. Lin, G. J. Ehlert, C. Bukowsky and H. A. Sodano, *ACS Appl. Mater. Interfaces*, 2011, **3**, 2200-2203.
334 C. C. Wang, H. C. Chen and S. Y. Lu, *Chem. Eur. J.*, 2014, **20**, 517-523.
335 S. Dubin, S. Gilje, K. Wang, V. C. Tung, K. Cha, A. S. Hall, J. Farrar, R. Varshneya, Y. Yang and R. B. Kaner, *ACS Nano*, 2010, **4**, 3845-3852.
336 J. X. Geng, L. J. Liu, S. B. Yang, S. C. Youn, D. W. Kim, J. S. Lee, J. K. Choi and H. T. Jung, *J. Phys. Chem. C*, 2010, **114**, 14433-14440.
337 G. Y. He, H. Q. Chen, J. W. Zhu, F. L. Bei, X. Q. Sun and X. Wang, *J. Mater. Chem.*, 2011, **21**, 14631-14638.
338 D. A. C. Brownson and C. E. Banks, *Phys. Chem. Chem. Phys.*, 2012, **14**, 8264-8281.
339 G. Q. Ning, C. G. Xu, Y. M. Cao, X. Zhu, Z. M. Jiang, Z. J. Fan, W. Z. Qian, F. Wei and J. S. Gao, *J. Mater. Chem. A*, 2013, **1**, 408-414.
340 X. C. Dong, P. Wang, W. J. Fang, C. Y. Su, Y. H. Chen, L. J. Li, W. Huang and P. Chen, *Carbon*, 2011, **49**, 3672-3678.
341 K. S. Kim, Y. Zhao, H. Jang, S. Y. Lee, J. M. Kim, K. S. Kim, J. H. Ahn, P. Kim, J. Y. Choi and B. H. Hong, *Nature*, 2009, **457**, 706-710.
342 T. Bhardwaj, A. Antic, B. Pavan, V. Barone and B. D. Fahlman, *J. Am. Chem. Soc.*, 2010, **132**, 12556-12558.